Full System Bifurcation Analysis of Endocrine Bursting Models

Krasimira Tsaneva-Atanasova[1]
Department of Engineering Mathematics,
University of Bristol, Bristol BS8 1TR, UK

Hinke M. Osinga
Department of Engineering Mathematics,
University of Bristol, Bristol BS8 1TR, UK,

Thorsten Rieß
Department of Engineering Mathematics,
University of Bristol, Bristol BS8 1TR, UK,

Arthur Sherman
Laboratory of Biological Modeling, NIDDK
NIH, Bethesda, MD

September 4, 2009

[1]Corresponding author. Address: Department of Engineering Mathematics, University of Bristol, Bristol BS8 1TR, UK, Tel.: +44 (0)117 331-6774, Fax: +44 (0)117 331-8093, Email: K.Tsaneva-Atanasova@bristol.ac.uk

Abstract

Plateau bursting is typical of many electrically excitable cells, such as endocrine cells that secrete hormones and some types of neurons that secrete neurotransmitters. Although in many of these cell types the bursting patterns are regulated by the interplay between voltage-gated calcium channels and calcium-sensitive potassium channels, they can be very different. For example, in insulin-secreting pancreatic β-cells, plateau bursting is characterized by well-defined spikes during the depolarized phase whereas in pituitary cells, bursting features fast, irregular, small amplitude spikes. The latter has been termed "pseudo-plateau bursting" because the spikes are transients around a depolarized steady state rather than stable oscillations in the fast subsystem. In this study we systematically investigate the bursting patterns found in endocrine cell models. We show that this class of voltage and calcium gated conductance based models can be reduced to the polynomial model of Hindmarsh and Rose (25). This reduction preserves the main properties of the biophysical class of models that we consider and allows for detailed bifurcation analysis of the full fast-slow system. Our analysis does not require decomposition of the full system into fast and slow subsystems and reveals properties of endocrine bursting that are not captured by the standard fast-slow analysis.

Key words: Excitable systems; Bifurcation theory; Bursting oscillations; Spike Adding; Endocrine Cells.

Introduction

Plateau bursting is an intrinsic property of endocrine cells by means of which they achieve the rise in intracellular calcium concentration necessary for secretion (4, 5, 29, 48). It is mediated via the interaction of voltage-gated calcium (Ca^{2+}) channels and various potassium (K^{+}) channels in the cell membrane. Upon stimulation that generally leads to depolarization, the membrane potential becomes more positive, opening the voltage-gated Ca^{2+} channels. The resulting Ca^{2+} influx into the cytosol triggers activation of calcium-sensitive potassium (K_{Ca}) channels, generating the outflow of K^{+} ions that repolarizes the membrane potential. This repolarization leads to closure of voltage-gated Ca^{2+} channels and subsequent decrease in the cytosolic calcium levels ($[\mathrm{Ca}^{2+}]_{\mathrm{i}}$). This sequence of events leads to oscillations in the intracellular calcium concentration that are accompanied by plateau-bursting electrical activity. Such prolonged electrical activity is an efficient way to increase intracellular Ca^{2+}, in contrast to brief neuron-like single spikes. The increase of $[\mathrm{Ca}^{2+}]_{\mathrm{i}}$ stimulates the release of hormones from secretory vesicles (4, 5, 29, 48). The plateau-bursting electrical activity is characterized by periodic switches between an active (depolarized) phase accompanied by increase in $[\mathrm{Ca}^{2+}]_{\mathrm{i}}$ and a silent (repolarized) phase during which $[\mathrm{Ca}^{2+}]_{\mathrm{i}}$ decreases due to Ca^{2+} extrusion. Owing to the importance of this activity, numerous modeling studies have been carried out of plateau-bursting in a variety of cell types, including pancreatic β-cells (11, 12, 16, 22, 46, 51) and pituitary cells (30, 40, 42, 45, 47). The models in these studies are generally derived using the Hodgkin-Huxley formalism (26) and generate bursting behavior by taking into account the crosstalk between voltage-dependent Ca^{2+} channels and K_{Ca} channels in combination with the slow dynamics of intracellular calcium concentration.

An important feature of plateau bursters is that the fast spikes during the active phase do not cross the baseline of the slow oscillation in the silent phase. There are two types of plateau-bursting patterns that have been found in models. The classical square-wave (10, 36) (or fold-homoclinic (27)) bursting is typical for pancreatic β-cells and is characterized by well-defined spikes in the active phase that correspond to stable limit cycle solutions in the fast subsystem of such models. The other type of plateau bursting is typical of pituitary cells (30, 40, 42, 45, 47) which exhibit small irregular spikes in the active phase. This pattern has been called pseudo-plateau bursting (40) because it is produced by transient oscillations rather than stable limit cycles, and has been classified mathematically as fold-subHopf (27). Despite these differences, the bursting patterns observed in endocrine cell models are both governed by the interplay between voltage-dependent Ca^{2+} channels and K_{Ca} channels.

The focus of this paper is investigation of these two plateau-bursting patterns.

We are interested in identifying fundamental properties of this class of models in terms of parameter(s) that control the behavior of the system. We consider a generic simplified biophysical model system (see Appendix A.1 for details) based on elements drawn from several published models (12, 42, 45). We show that a model system of the above class can generate both types of plateau bursting, depending on the balance between inward and outward currents. We begin by performing a classical fast-slow bifurcation analysis (36) of the generic model and demonstrate how the transition between square-wave and pseudo-plateau bursting takes place in the 'frozen' fast subsystem. We then go beyond the fast-slow analysis to examine bifurcations of the full bursting system with respect to the speed of the slow variable. This is of particular interest for fold-subHopf bursting, which produces appropriate spiking patterns when the separation of time-scales is not extreme.

In order to facilitate the computations and demonstrate the generality of the results, we employ a polynomial reduction of Hindmarsh-Rose type (25). We demonstrate that this model, although phenomenological, duplicates the qualitative behavior of the biophysical system in the frozen case and then use it to study systematically the full-system bifurcations that lead to bursting and that control the number of spikes per burst. We follow representative periodic orbits of the full ODE system with different numbers of spikes and find that the same patterns of bifurcations govern both square-wave and pseudo-plateau periodic solutions. Most interestingly, we find for both classes of bursters that the patterns differ depending on the location of the full-system steady state, which lies on a branch of saddle equilibria in the fast subsystem, relative to the homoclinic orbit of the fast subsystem.

Fold-homoclinc bursting has been previously studied and others have similarly pointed out the central role of bifurcations of the full system (2, 39, 50). One study (7) has demonstrated locally the emergence of such bursting oscillations from homoclinic connections in the limit $\epsilon \to 0$. None of these studies, however, has treated the case of fold-subHopf bursting nor systematically compared it to fold-homoclinic bursting.

Results

Generic Endocrine System

Since the pioneering work of Rinzel (36), it has become a standard approach to study bursting oscillations using fast-slow analysis, i.e. by decomposing the model into fast and (one-dimensional) slow subsystems and analyzing the dynamics of the full system in the limit of the slow variable treated as a bifurca-

tion parameter. In the class of models (Appendix A.1) that we consider, the only slow variable is the cytosolic calcium concentration (c), which indeed changes much more slowly than the membrane potential (V_{m}) and the channel gating variables. The separation of time scales in these models is controlled by the parameter f_{c}, which represents the fraction of free $[\mathrm{Ca}^{2+}]_{\mathrm{i}}$. Fast-slow analysis has been widely used in theoretical studies of both square-wave and pseudo-plateau bursters (10, 12, 30, 36, 40, 42, 43, 45), assuming that $[\mathrm{Ca}^{2+}]_{\mathrm{i}}$ is a slow variable. These studies have shown that square-wave bursting models are characterized by a supercritical Hopf bifurcation in the fast subsystem, whereas in pseudo-plateau bursters this bifurcation is subcritical. We illustrate this in Fig. 1 using the generic endocrine model (Appendix A.1), where we vary the half-maximum activation $V_{\mathrm{m_L}}$ of the voltage-gated Ca^{2+} channels in order to change the type of the Hopf bifurcation of the fast subsystem (Eqns. (4)–(5)). We also superimpose the bursting trajectories of the full system for each value of $V_{\mathrm{m_L}}$ on the corresponding bifurcation diagrams.

For $V_{\mathrm{m_L}} = -22.5$ mV, illustrated in Fig. 1(a), the generic model behaves like a typical model for pancreatic β-cell square-wave bursting (10, 12, 36, 43). Note that the simplified generic model corresponds to classical bursting with cytosolic Ca^{2+} as the single slow variable, which is exemplified by the original Chay-Keizer model (16). More recent β-cell models incorporate effects of Ca^{2+} in the endoplasmic reticulum and ATP (12), but we neglect these as they have no analog in models of pituitary bursting. As shown in Fig. 1(a), the fast subsystem is bi-stable for a range of values of the control parameter c, and is characterized by a Z-shaped steady-state curve that folds at saddle-node bifurcation points labeled SN_1 and SN_2. The upper branch of this curve consists of stable foci that lose stability as calcium increases via a supercritical Hopf bifurcation (HB). Between HB and SN_1 the upper branch points are unstable foci/nodes that become saddles at SN_1. The steady state gains stability again at SN_2 and beyond this point it is a stable node. The Hopf bifurcation gives rise to a branch of stable periodic orbits that terminates in a homoclinic bifurcation (HC) with one of the saddles on the steady-state branch delimited by the two saddle-node bifurcations SN_1 and SN_2. Bursting also relies on the fact that the c-nullcline of the full system Eqns. (4)–(6) (not shown in Fig. 1) intersects the Z-shaped steady-state curve of the fast subsystem Eqns. (4)–(5) somewhere in the middle branch. Thus, the membrane potential (V_{m}) in the full system periodically switches between silent and active phases due to repeated intersections of the bursting trajectory and the c-nullcline that force it to change direction in the phase space.

For the case $V_{\mathrm{m_L}} = -27.5$ mV shown in Fig. 1(b), the bifurcation curves closely resemble those from several pituitary bursting models (30, 40, 42, 45). Compared with the case for $V_{\mathrm{m_L}} = -22.5$ mV, we observe that the 5 mV left

shift in the Ca^{2+} current activation curve preserves the Z-shaped steady-state curve of the fast subsystem Eqns. (4)–(5) along with its stability properties, but it has shifted to the right. Furthermore, the Hopf bifurcation of the fast subsystem is now subcritical, which results in a branch of unstable periodic orbits that terminates at HC. As can be seen from the trajectory of the full system Eqns. (4)–(6) shown in Fig. 1(b), the transition in the type of the Hopf bifurcation results in pseudo-plateau rather than square-wave bursting, as the spikes are due to a slow oscillatory approach to the upper steady-state branch, not stable limit cycles. Such spikes can only occur if $[\mathrm{Ca}^{2+}]_{\mathrm{i}}$ is not too slow. Specifically, the rate of increase of $[\mathrm{Ca}^{2+}]_{\mathrm{i}}$ cannot be much slower than the rate of approach of the solution to the upper steady state. Indeed, pseudo-plateau bursters can lose bursting oscillations when the slow variable is made too slow, if the trajectory is absorbed in a stable state on the upper branch of the Z-curve. When the slow variable is faster, however, bursting is possible because the trajectory exits the active phase before reaching the stable steady-state. In the class of plateau-bursting models that we focus on, the parameter f_{c} that controls the separation of time scales typically ranges from 10^{-3} to 10^{-1} (11, 12, 16, 30, 40, 42, 45–47), which is only moderately small.

For intermediate values of $V_{\mathrm{m_L}}$ (not shown), the bifurcation diagram of the fast subsystem Eqns. (4)–(5) deforms continuously via a (codimension-two) degenerate Hopf bifurcation point, where HB changes from supercritical to subcritical. At first, the branch of unstable periodic orbits turns around at a saddle-node of periodics (SNP) bifurcation, which leads to a branch of stable limit cycles that terminates at HC. As $V_{\mathrm{m_L}}$ decreases and the Z-curve shifts to the right, the point HB also shifts to the right, but to a greater extent and, thus, moves closer to SN_1 and the middle branch of the Z-curve. Hence, eventually the SNP and HC occur simultaneously, after which the periodics never become stable.

The changes in the bifurcation diagrams in Fig. 1 reflect several biophysical effects of the left shift of the Ca^{2+} current activation curve, which alters the balance between Ca^{2+} and K^{+} currents in the inward direction. This means that more K_{Ca} current is needed to repolarize the bursts, so that the Z-curve shifts to the right. The shift of the HB reflects an enlarged region of conduction block, in which excessive inward current prevents spiking and results in a depolarized plateau. Note that the loss of true spiking increases the Ca^{2+} concentration because the mean membrane potential is higher without the hyperpolarized inter-spike interval. The model thus suggests that the levels of intracellular calcium concentration ($[\mathrm{Ca}^{2+}]_{\mathrm{i}}$) during pseudo-plateau bursting should be significantly greater than during square-wave bursting (Fig. 1), in accord with published experimental data showing simultaneous recordings of voltage (V_{m}) and cytosolic calcium concentration ($[\mathrm{Ca}^{2+}]_{\mathrm{i}}$) in pancreatic β-cells (see Fig. 2 in (5)) and pituitary cells (see Fig. 5 in (48) and Fig. 1 in (45)). According to these studies, calcium levels in pancreatic β-cells

oscillate between 0.15 μM and 0.35 μM, whereas in pituitary cells $[\mathrm{Ca}^{2+}]_{\mathrm{i}}$ can exceed 1 μM during bursts.

The Polynomial Model

We complement the classical fast-slow analysis with a bifurcation analysis of the full system. Such a full-system analysis provides a different view of the bursting solution as a periodic orbit with a complicated internal structure. This approach is necessary to detect chaos, which, as shown by Terman (44), is more robust when the slow variable is not very slow and thus is more likely to be observed in experiments. In order to investigate systematically the full system bifurcation structure of endocrine models we construct a polynomial plateau-bursting model by building into it the common dynamical features found in a number of biophysical modeling studies (2, 11, 12, 30, 34, 40, 42, 43, 45, 46).

Equations and Assumptions

The polynomial model is a modified Hindmarsh-Rose type model (25) with parameters chosen such that the bifurcation diagram of the fast subsystem is similar to that of Eqns. (4)–(5), that is, the upper steady-state branch exhibits a single Hopf bifurcation; compare also (39). The equations have the general form

$$\frac{dx}{dt} = f(x,y,z), \tag{1}$$

$$\frac{dy}{dt} = \phi g(x,y), \tag{2}$$

$$\frac{dz}{dt} = \epsilon h(x,z), \tag{3}$$

where $f(x,y,z)$, $g(x,y)$ and $h(x,z)$ for $(x,y,z) \in \mathbb{R}^3$ are sufficiently smooth functions and ϕ and ϵ are rate constants that govern the separation of time scales. The variable $x(t)$ represents the membrane potential and the other two variables $y(t)$ and $z(t)$ stand for the gating dynamics of the (K^+) channels and the dynamics of cytosolic Ca^{2+}, respectively. We require the right-hand sides to satisfy the following conditions:

C1 The function $f(x,y,z) = -s\,(-a\,x^3 + x^2) - y - b\,z$ is a cubic function that guarantees an N-shaped x-nullcline. Since $x(t)$ acts in place of the membrane potential (Eqn. (4) in Appendix A.1), the term $s\,a\,x^3$ represents the contribution of the Ca^{2+} inward current; $-x^2 - y$ represents the contribution of the outward voltage sensitive K^+ currents; and $-b\,z$ stands for the contribution of the outward calcium-sensitive potassium current.

C2 The function $g(x, y) = x^2 - y$ is a quadratic function that gives a parabolic y-nullcline and replaces the delayed rectifier activation kinetics (Eqn. (5) in Appendix A.1). It depends only on the membrane potential and is, therefore, decoupled from the third Eqn. (3).

C3 The function $h(x, z) = s\,a_1\,x + b_1 - k\,z$ is linear in x and z and represents Ca^{2+} dynamics, with the term $s\,a_1\,x + b_1$ replacing the source of calcium through voltage-gated calcium Ca^{2+} channels and $-k\,z$ standing for the decay term in Eqn. (6).

C4 The time-scale paramters ϕ and ϵ are such that x and y vary on a faster time scale than z. Although strictly speaking in the biophysical system Eqns. (4)–(6) there are three different intrinsic times scales for V_{m}, n and c, it has usually been assumed that V_{m} and n are fast variables compared to c. This is a reasonable assumption given that the time scale of change in Ca^{2+} concentrations is several orders of magnitude smaller than V_{m} and n. Therefore, in the polynomial model we take $\phi = 1$ and consider ϵ a small positive parameter.

C5 The parameters $a, b \geq 0$ in the fast subsystem Eqns. (1)–(2) of the polynomial model are chosen, without loss of generality (W.L.O.G.), such that for a range of values of $z \geq 0$ there are three equilibrium points (x_i^e, y_i^e), $i = 1, 2, 3$, given by the points of intersection of the x- and y-nullclines. Furthermore, we require that these equilibria are of the following type: (x_1^e, y_1^e) is a stable focus, (x_2^e, y_2^e) is a saddle, and (x_3^e, y_3^e) is a stable node. These conditions ensure that the fast subsystem Eqns. (1)–(2) of the polynomial model has a Z-shaped steady-state curve defined by $\{y = x^2$ and $z = \left(s\,a\,x^3 - (s+1)\,x^2\right)/b\}$ that guarantees a region of bistability for a range of values of $z \geq 0$ (Fig. 2).

C6 The parameters $a_1, b_1 \leq 0$ and $k \geq 0$ in the (one-dimensional) slow subsystem Eqn. (3) of the polynomial model are chosen W.L.O.G. such that the z-nullcline $\{z = (s\,a_1\,x + b_1)/k\}$, intersects the Z-shaped steady-state curve $\{y = x^2$ and $z = \left(s\,a\,x^3 - (s+1)\,x^2\right)/b\}$ of the fast subsystem Eqns. (1)–(2) somewhere in the middle branch, which is of saddle type (Fig. 2). This intersection point corresponds to a degenerate branching bifurcation of the full system Eqns. (1)–(3) at $\epsilon = 0$ and it determines the location and stability of the equilibrium $\mathrm{FP} = (x_{\mathrm{FP}}, y_{\mathrm{FP}}, z_{\mathrm{FP}})$ of the full system that persists for $\epsilon > 0$; see Appendix A.2 for details.

C7 Plateau bursting also relies on the existence of a Hopf bifurcation in the fast subsystem (Eqns. (1)–(2)); we assume that this Hopf bifurcation is unique. The parameter $s < 0$ in the polynomial model Eqns. (1)–(3) plays the same role as $V_{\mathrm{m_L}}$ in the generic endocrine model Eqns. (4)–(6); it controls the type of bursting by converting the Hopf bifurcation (HB) of the fast subsystem from supercritical to subcritical (Fig. 2). The type of HB is determined by

the sign of a first Lyapunov coefficient evaluated at the critical equilibrium $(x_{\rm HB}, y_{\rm HB}) = (x_{\rm HB}, x_{\rm HB}^2)$, and in our case (28) it is given by:

$$\begin{aligned} \mathrm{sign}\left[l_1(x_{\rm HB})\right] &= \mathrm{sign}\left[F''' + \tfrac{F''(F''-G'')}{(G'-\phi)}\right] \\ &= \mathrm{sign}\left[6\,s\,a + \tfrac{(2\,s\,(3\,a\,x_{\rm HB}-1))^2 - 2\,(2\,s\,(3\,a\,x_{\rm HB}-1))}{2\,x_{\rm HB}-1}\right], \end{aligned}$$

where $F(x) = -s\,(-a\,x^3 + x^2) - b\,z$ and $G(x) = x^2$. The values of $s < 0$ that we consider are chosen W.L.O.G. such that this transition occurs in the region of bistability with respect to z (Fig. 2).

In the following analysis we fix all the parameters in the model except for ϵ, s and b_1. The parameter ϵ controls the speed of the slow variable z and is our main bifurcation parameter corresponding to $f_{\rm c}$ in the generic endocrine model. The parameter s controls the location and type of HB in the fast subsystem, which is also related to the position of the HC, in analogy with the effect that decreasing $V_{\rm m_L}$ has on the behavior of the generic endocrine system (Fig. 1). Note that, similar to $V_{\rm m_L}$, the parameter s also appears in the slow (z) equation of the polynomial model. The parameter b_1 determines the location of the equilibrium $\mathrm{FP} = (x_{\rm FP}, y_{\rm FP}, z_{\rm FP})$ of the full system, which exists for all ϵ and is given by the intersection of the z-nullcline and the Z-shaped steady-state curve of the fast subsystem Eqns. (1)–(2); the locus of FP affects the bifurcations of the full system Eqns. (1)–(3) that occur when ϵ is varied. Without loss of generality and according to conditions **C**1–**C**7 we choose the rest of the system parameters to be: $a = 0.5$, $b = 1$, $a_1 = -0.1$ and $k = 0.2$.

We plot in Fig. 2 the bifurcation diagram of the polynomial fast subsystem Eqns. (1)–(2) using the slow variable z as bifurcation parameter; panel (a) shows the bifurcation diagram for $s = -1.61$ and panel (b) for $s = -2.6$, which correspond to square-wave and pseudo-plateau bursting, respectively. A comparison between Figs. 1 and 2 demonstrates that the polynomial model reproduces qualitatively the dynamics of the generic endocrine model. Similar to the biophysical system, the transition from supercritical to subcritical Hopf bifurcations in the fast subsystem of the phenomenological model Eqns. (1)–(3) is accompanied by a right shift of the Z-shaped steady-state curve that, consequently, covers a larger range of z-values during plateau bursting in the full system. In both panels of Fig. 2 we also plot the z-nullclines for values of b_1 where they intersect the Z-curve below, near, and well above the homoclinic bifurcation (HC) of the fast subsystem.

Bifurcation Analysis of the Full System

The equilibria and periodic orbits found in the polynomial fast subsystem Eqns. (1)–(2) can also be thought of as equilibria and periodic orbits of the full system Eqns. (1)–(3), but they only exist for $\epsilon = 0$ and the full system is degenerate here. Therefore, we cannot expect that all equilibria and periodic orbits persist for $\epsilon > 0$. In fact, only one of the equilibria survives, namely the steady state $\mathrm{FP} = (x_{\mathrm{FP}}, y_{\mathrm{FP}}, z_{\mathrm{FP}})$ on the Z-shaped curve at which the z-nullcline intersects the bifurcation diagram of the fast subsystem. Clearly, if this intersection lies on the lower branch of stable equilibria or on the upper branch such that the corresponding equilibrium in the fast subsystem is stable then the full system does not support any bursting or spiking solutions. Indeed, for these cases FP is a globally stable equilibrium for $\epsilon > 0$ (Appendix A.2). However, if FP for $\epsilon = 0$ corresponds to an unstable equilibrium of the fast subsystem, then a small perturbation $\epsilon > 0$ may give rise to a periodic orbit of the full system, which corresponds to a bursting or spiking orbit (7, 44). Unfortunately, this theory only gives predictions for $0 < \epsilon \ll 1$.

We perform a numerical continuation study of the full system Eqns. (1)–(3) and study how the periodic orbits of the full system are organized for a much larger range of $\epsilon > 0$. We consider both square-wave and pseudo-plateau bursting, for $s = -1.61$ and $s = -2.6$, respectively (Figs. 3–6). We find that the steady state FP, which does not depend on ϵ, gains stability at an $\mathrm{O}(1)$-value of $\epsilon > 0$ in a Hopf bifurcation (HB_2). The emanating branch of periodic orbits of the full system gives rise to a sequence of spike-adding bifurcations. The nature of this sequence is determined only by the location of FP relative to the homoclinic bifurcation HC of the fast subsystem. In order to illustrate this, we will use the parameter b_1 to shift the locus of FP below and above the HC (Fig. 2) and compute the respective bifurcation diagrams of the full model Eqns. (1)–(3) for both types of bursting. While the bifurcations SN_1, HB (labeled HB_1 in Figs. 3–6), HC and SN_2 of the fast subsystem (Fig. 2) do not persist for $\epsilon > 0$, we will show later that HB_1 and SN_2 for special values of b_1 act as end points of a curve in (ϵ, b_1)-space that corresponds to Hopf bifurcations HB_2 of the full system (see Fig. 10).

Route to Bursting via Spike-Adding Saddle-Node of Periodics Bifurcations. We start our analysis of the bifurcation structure of the polynomial system Eqns. (1)–(3) by considering the case $b_1 = -0.01$, for which FP lies below HC. Figure 3 shows the bifurcation diagram of the full system for $s = -1.61$ and Fig. 4 for $s = -2.6$. The bifurcation diagrams are presented in three-dimensional (ϵ, z, x)-space with ϵ as the bifurcation parameter plotted on a logarithmic scale in panels (a) and on an (enlarged) linear scale in panels (b). We also plot the bifurcation dia-

grams of the fast subsystems Eqns. (1)–(2) for $\epsilon = 0$. Since on the logarithmic scale these would be pushed off to $-\infty$, we project them onto the (z, x)-plane at an arbitrary fixed value of $\epsilon = 10^{-7}$.

The unique equilibrium FP of the full system Eqns. (1)–(3), which has real eigenvalues $\lambda_1 < 0 < \lambda_2$ and $\lambda_3 = 0$ at $\epsilon = 0$, becomes a hyperbolic saddle and $\lambda_3 > 0$ for $\epsilon > 0$ small (Appendix A.2). As ϵ increases, FP becomes stable in a Hopf bifurcation (HB_2). The Hopf bifurcation HB_2 is subcritical both for $s = -1.61$ (Fig. 3) and $s = -2.6$ (Fig. 4) and gives rise to a branch of unstable periodic orbits that becomes stable in a saddle-node of periodics (SNP_1). The branch of stable periodic orbits corresponds to tonic spiking of large amplitude, unlike the tonic spiking typically seen in β-cell models as the Ca^{2+} pump rate is increased (36, 44) or the conductance of K_{Ca} channels is decreased (15, 31). This branch can be considered as bursts with one spike. Sample spiking trajectories of the full system are superimposed on the bifurcation diagrams in Figs. 3(b) and 4(b). The first one (from the right) in both figures is a two-spike periodic orbit. As ϵ decreases, the branch of one-spike periodic orbits loses and regains stability in saddle-node of periodics (SNP) bifurcations and during this process it transforms from a one-spike into a two-spike periodic orbit. The transition happens over a very narrow range of ϵ, to the right of SNP_2, during which the stable one-spike periodic orbit coexists with a stable two-spike periodic orbit. As ϵ decreases further the series of SNP bifurcations repeats, delimiting smaller and smaller portions of the branch, each of which corresponds to a bursting solution with one more spike (Figs. 3 and 4). Using the software package AUTO (17), we were able to follow this branch down to ϵ of order 10^{-3}. Figures 3(b) and 4(b) illustrate the accumulation of the SNP bifurcations as ϵ decreases for square-wave ($s = -1.61$) and pseudo-plateau ($s = -2.6$) bursting, respectively. The bifurcation diagrams for square-wave and pseudo-plateau bursting are very similar and both exhibit a sequence of SNP bifurcations creating n-spike solutions for increasingly larger n as ϵ decreases. In the limit $\epsilon \to 0$ the number of spikes of the stable bursting solutions goes to infinity, while the stability region of each individual orbit goes to zero. This phenomenon can be regarded as a spike-adding cascade (2, 7, 34, 50).

Figures 3 and 4 suggest that the full system exhibits a spike-adding cascade mediated by SNP bifurcations if the equilibrium point FP of the full system lies below the homoclinic bifurcation HC of the fast subsystem for $\epsilon = 0$ (Figs. 2(a) and (b) with $b_1 = -0.01$).

Route to Bursting via Spike-Adding Isolas. We continue our analysis of the bifurcation structure of the polynomial model Eqns. (1)–(3) by considering the cases $b_1 = -0.045$, $s = -1.61$ and $b_1 = -0.21$, $s = -2.6$, for which FP lies

above HC (Figs. 5 and 6, respectively). As before, we use ϵ as the bifurcation parameter and plot the bifurcation diagrams of the full system in (ϵ, z, x)-space on a logarithmic scale in panels (a) and on an (enlarged) linear scale in panels (b). The bifurcation diagrams of the fast subsystems Eqns. (1)–(2) for $\epsilon = 0$ are plotted as well; for the logarithmic-scale pictures in Figs. 5(a) and 6(a) they are projected onto the (z, x)-plane at the arbitrary values of $\epsilon = 10^{-4}$.

Our choices for b_1 and s illustrate the two possibilities for positioning the unique equilibrium FP of the full system Eqns. (1)–(3). For $b_1 = -0.045$ and $s = -1.61$ the z-nullcline intersects the bifurcation diagram of the fast subsystem above HC, but below SN_1. For $b_1 = -0.21$ and $s = -2.6$, on the other hand, this intersection lies in between SN_1 and HB_1; compare Figs. 2(a) and (b). As before, if FP lies in between HC and SN_1, it has real eigenvalues $\lambda_1 < 0 < \lambda_2$ and $\lambda_3 = 0$ at $\epsilon = 0$ and becomes a hyperbolic saddle and $\lambda_3 > 0$ for $\epsilon > 0$ small (Appendix A.2). However, if FP lies in between SN_1 and HB_1, the eigenvalues from the fast subsystem are unstable; they are real for FP close to SN_1 and form a complex conjugate pair for FP close to HB_1. In this case $\lambda_3 < 0$ and FP is again a hyperbolic saddle with two unstable eigenvalues for $\epsilon > 0$ small (Appendix A.2).

We find that the bifurcation diagram of the full system is topologically equivalent for these two choices of FP above HC, but rather different from the case where FP lies below HC. Note that, locally near $\epsilon = 0$, there is no difference in whether FP lies below or above HC; as ϵ increases FP becomes a hyperbolic saddle with two unstable eigenvalues and it gains stability in a Hopf bifurcation (HB_2). However, in contrast to Figs. 3 and 4, the Hopf bifurcation HB_2 is now supercritical and gives rise to a branch of stable periodic orbits that correspond to large-amplitude tonic spiking. As before, we superimpose sample spiking trajectories of the full system on the bifurcation diagrams in Figs. 5(b) and 6(b) and an example of a stable one-spike periodic orbit is shown in Fig. 6(b), where $s = -2.6$.

Both for $s = -1.61$ and $s = -2.6$ the branch of one-spike periodic orbits loses stability in a supercritical period-doubling bifurcation (PD_1). The emanating branch of stable period-doubled orbits corresponds to two-spike periodic orbits, examples of which are superimposed on the bifurcation diagrams in Figs. 5(b) and 6(b). The two-spike periodic orbit loses stability in another period-doubling bifurcation (PD_2) that gives rise to a period-doubled two-spike orbit; an example of such a periodic orbit is shown in Fig. 5(b) and we can clearly see that it does not correspond to a standard bursting solution. The period-doubled two-spike orbit is stable for a much smaller range in ϵ and it also loses stability in a period-doubling bifurcation, starting a period-doubling cascade (not shown). We will refer to these and further period-doubled n-spike orbits as secondary bursting solutions and we do not pursue further investigation of these types of period-doubling cascades.

Instead, we focus on the spike-adding cascade that occurs also if FP lies above

HC. In this case, the spike-adding cascade is organized by isolas. A family of stable n-spike periodic orbits is born in an SNP bifurcation and, as ϵ decreases, it undergoes period-doubling bifurcations to secondary bursting solutions. We found these isolas by generating seed solutions using numerical integration of Eqns. (1)–(3) for decreasing fixed values of ϵ and continuing them in AUTO (17). Figures 5 and 6 show isolas of n-spike periodic orbits for $n = 3, \ldots, 9$ and $n = 3, \ldots, 12$, respectively, along with examples of bursting trajectories with increasing numbers of spikes. We observe that the isolas create gaps between stable n-spike periodic orbits for moderately small values of ϵ, but they overlap as ϵ decreases creating narrow intervals with coexisting stable n- and $(n+1)$-spike periodic orbits. However, the stable portions of the isolas become smaller as n increases resulting in smaller regions in parameter space where each stable n-spike periodic orbits exist.

Figures 5 and 6 suggest that the full system exhibits a spike-adding cascade mediated by period-doubling bifurcations and isolas if the equilibrium point FP of the full system lies above the homoclinic bifurcation HC of the fast subsystem for $\epsilon = 0$ (Figs. 2(a) and (b) with $b_1 = -0.045$ and $b_1 = -0.21$, respectively). In particular, it does not seem to matter whether FP lies below or above the saddle-node bifurcation SN_1 of the fast subsystem for $\epsilon = 0$ as long as the corresponding equilibrium of the fast subsystem is unstable.

Chaotic Bursting Solutions When the route to bursting is mediated via spike-adding SNP bifurcations (FP well below HC), periodic bursting is accompanied by bistability and chaotic alternation between regular n- and $(n+1)$-spike periodic orbits. This has previously been shown for fold-homoclinic bursting (43), and an example of irregular, presumably chaotic, alternation between two- and three-spike solutions is illustrated for fold-subHopf bursting in Fig. 7(a). In contrast, when bursting arises via spike-adding isolas (FP well above HC), bursting can be chaotic due to the overlapping of isolas in regimes where period-doubling cascades exist. These give rise to chaotic alternations between regular n-spike periodic orbits and secondary bursting solutions. As an illustration of such behavior, we plot in Fig. 7(b) a time series of the polynomial model in the fold-homoclinic case, showing a spontaneous transition from period-doubled two-spike solutions to three-spike bursting.

Mixed Route to Bursting. When FP lies close to the HC for $\epsilon = 0$, the periodic solutions branches are of mixed type. As an illustration we computed the bifurcation diagrams of the full system Eqns. (1)–(3) both for the cases of fold-homoclinic bursting, with $s = -1.61$ and $b_1 = -0.023$ (Fig. 2(a)), and of fold-subHopf bursting, with $s = -2.6$ and $b_1 = -0.066$ (Fig. 2(b)).

The fold-homoclinic case is shown in Fig. 8(a) and corresponds to a situation where FP lies just below the HC for $\epsilon = 0$. In contrast to Fig. 3, the Hopf bifurcation HB_2 is supercritical and gives rise to a branch of stable one-spike periodic orbits that ends at a period-doubling bifurcation (PD_1). For these relatively large values of ϵ, the bifurcation diagram resembles that of Fig. 5: a branch of stable two-spike periodic orbits emanates from PD_1 that loses stability in another period-doubling bifurcation (PD_2), which gives rise to secondary bursting solutions. In a narrow ϵ-interval these secondary bursting solutions coexist with a branch of stable three-spike periodic orbits. As for Fig. 5, we did not further investigate the period-doubling cascade of secondary bursting solutions, but rather concentrated on the spike adding. The branch of three-spike periodic orbits (*magenta* curve) in Fig. 8(a) does not lie on an isola, in contrast to Fig. 5. For these smaller values of ϵ the bifurcation diagram resembles that of Fig. 3, as expected. Instead of individual isolas, continuation of the three-spike periodic orbits leads to a single connected branch of n-spike periodic orbits that consists of increasing numbers of spikes as ϵ decreases. We were able to follow this branch down to values of ϵ of order $O(10^{-3})$.

The fold-subHopf case is shown in Fig. 8(b) and corresponds to a situation where FP lies slightly above HC for $\epsilon = 0$. Here, HB_2 is also supercritical and the stable branch of one-spike periodic orbits again loses stability in a period-doubling bifurcation (PD). However, the emanating branch of stable two-spike periodic orbits undergoes a sequence of SNP bifurcations corresponding to a spike-adding cascade and the entire family of periodic orbits in the full system forms a single connected branch. As before we were only able to follow the branch down to values of ϵ of order $O(10^{-3})$.

The above computations indicate that there is an interesting transition between the two routes to bursting in both classes of models as FP crosses from one side of HC to the other. Detailed investigation of this transition is left for future investigation, because it requires numerical exploration in a region of very small values of ϵ where our computations break down.

Behaviour in the limit of small ϵ.

We have studied the case of $\epsilon = 0$ (fast subsystem bifurcations) and the cascade of periodic orbit bifurcations as ϵ decreases from large values, but it is evident that there are important phenomena in the region of small ϵ that our numerical continuations have not addressed. As mentioned earlier, Terman (44) and Belykh et al. (7) provide a theory for analyzing what type of periodic orbit of the full system arises from very small perturbations $\epsilon > 0$, but the theory in (7, 44) only applies to the case where FP is located just below or above the HC at $\epsilon = 0$. We

discuss here how their theory ties in with our numerical study for a much larger range of ϵ, including other locations for FP.

The limit of small ϵ for square-wave bursting Let us first consider square-wave (fold-homoclinic) bursting, which is Scenario 3 in (7). Terman (44) considered this case already in 1992, but we will follow Belykh et al. (7). If FP lies just below the HC (the case $l < 0$ in (7)), then there exists a bursting solution for $\epsilon > 0$ small enough. In the limit $\epsilon \to 0$ this bursting solution accumulates on a periodic orbit with infinitely many spikes and the range of the slow variable (z in our case) covers the interval between the lower saddle-node bifurcation SN_2 and the HC (7). The continuations shown in Figs. 3 and 8(a) indicate that there indeed exists a single connected branch of n-spike periodic orbits as $\epsilon \to 0$. While the continuation in ϵ only reaches values of order $O(10^{-3})$, direct numerical simulations indicate that bursting solutions persist and that their numbers of spikes and their periods increase to infinity in the limit of $\epsilon = 0$. Note that the theory in (7) is only valid for FP just below the HC, but our numerical study indicates that the bifurcation structure for $0 < \epsilon \ll 1$ remains the same also for FP closer to SN_2.

If FP lies just above the HC then Belykh et al. (7) predict the existence of an interval $0 < \epsilon \ll 1$ where continuous (tonic) spiking exists. This tonic spiking is a periodic orbit with an amplitude that is close to the homoclinic orbit at HC for $\epsilon = 0$ and it is different from the branch of large-amplitude tonic spiking solutions that we found emanating from the Hopf bifurcation HB_2 at large ϵ. The periodic orbit for $0 < \epsilon \ll 1$ may lose stability in a period-doubling bifurcation, but it definitely does not persist beyond an SNP bifurcation that is predicted to occur for some value $\epsilon \ll 1$. Belykh et al. go on to explain that bursting oscillations only occur after a homoclinic bifurcation of the full system, where the one-dimensional stable manifold of FP is contained in its two-dimensional unstable manifold. This homoclinic bifurcation happens at a value of ϵ that lies before the SNP bifurcation where the periodic orbit corresponding to tonic spiking is guaranteed to disappear if it has not lost stability already.

The theory again only applies when FP lies just above HC. In particular, for fixed small $0 < \epsilon \ll 1$, both Terman (44) and Belykh et al. (7) predict that a continuous variation from FP above the HC to FP below the HC (in our case this means increasing the parameter b_1) leads to a transition from continuous spiking to bursting via a regime with chaotic dynamics. If we continue moving FP further away above the HC, we expect that continuous spiking persists for increasingly larger values of $0 < \epsilon \ll 1$. The periodic orbit that corresponds to tonic spiking emanates from a closed curve at $\epsilon = 0$ that is some sort of average of a small family of the stable periodic orbits in the fast subsystem, where the range of the

family depends on where the z-nullcline intersects this family; see (39). Note that this argument also holds in the range for b_1 such that FP lies in between HB_1 and SN_1 at $\epsilon = 0$.

Unfortunately, in our numerical study we were unable to find the bifurcations that are predicted by the theory. Starting the continuation from the family of one-spike periodic orbits that emanates from HB_2 at relatively large ϵ, we found a route to bursting that is mediated via spike-adding isolas (Fig. 5). Note that the isolas overlap as ϵ decreases, which creates the possibility for chaotic motion with an unpredictable number of spikes within each burst (50). The family of stable n-spike periodic orbits in each isola is born in an SNP bifurcation at a maximal value of ϵ and loses stability in a period-doubling bifurcation for some smaller ϵ-value. However, this structure does not match the order of the bifurcations expected for the stable tonic spiking that is predicted to exist for $0 < \epsilon \ll 1$. Therefore, we conjecture that the homoclinic bifurcation of FP at a value $0 < \epsilon \ll 1$ gives rise to the family of isolas. The precise value of ϵ for which this homoclinic bifurcation in the full system occurs depends on the distance between FP and the HC at $\epsilon = 0$. Interestingly, in the case $b_1 = -0.045, s = -1.61$ (Fig. 5) the limiting homoclinic orbit appears to have the same amplitude as the homoclinic orbit of the fast subsystem, but this also appears to be the case for the families of unstable periodic orbits in Fig. 8(a), where FP lies below the HC. Hence, our numerical study is inconclusive here.

The limit of small ϵ for pseudo-plateau bursting The analysis for the range $0 < \epsilon \ll 1$ for pseudo-plateau (fold-subHopf) bursting has not been done. Pseudo-plateau bursting in the biophysical sense (small transient spikes) relies on the fact that ϵ is only moderately small, but the fold-subHopf structure persists for very small epsilon. For such very small values of ϵ, the case of fold-subHopf bursting compares to Scenario 1 in (7), that is, for $0 < \epsilon \ll 1$ the solutions are relaxation oscillations determined by the branches of stable equilibria; for Scenario 1 the two branches of stable equilibria end at the saddle-node bifurcations SN_1 and SN_2, but in our case the upper equilibrium branch loses stability already at the subcritical Hopf bifurcation HB_1. Hence, we expect the scenario of slow passage through a Hopf bifurcation (3) and the bursting solutions for $0 < \epsilon \ll 1$ resemble relaxation oscillations with many small-amplitude oscillations during the active phase that first decrease and subsequently increase in amplitude.

We point out that the theory for $0 < \epsilon \ll 1$ in the case of fold-subHopf bursting is the same for FP below or above the HC, and it equally does not matter whether b_1 is such that FP lies in between HB_1 and SN_1 at $\epsilon = 0$. Hence, for very small ϵ one expects that the spike-adding cascades organized by both SNP bifurcations (Fig. 4)

and isolas (Fig. 6) transform to a topologically equivalent bifurcation structure. Considering the case where the bifurcation diagram is of mixed type (Fig. 8(b)), it seems likely that the bursting solutions eventually form a single connected branch of periodic orbits with a spike-adding cascade organized by SNP bifurcations as ϵ decreases. This raises the question whether this could also be the case for fold-homoclinic bursting, despite the fact that for that case it does matter whether FP lies above or below the HC. Again, our numerical study is inconclusive here and a detailed investigation is left for future work.

Nevertheless, we can get a glimpse into the region with $0 < \epsilon \ll 1$ via selected numerical integrations in time. Inspection of the slow variable (z) oscillations for fold-subHopf bursting indeed suggests persistence of slow oscillations with periods going to infinity. The delayed passage through the Hopf bifurcation HB_1 is characterized by the fact that the maximum of z lies at the same distance from the z-value of HB_1 as its minimum. If HB_1 lies too close to SN_1 then the maximum of z equals the z-value of SN_1. Figure 9(a) illustrates this for the polynomial model with $s = -2.6$, $b_1 = -0.01$ and $\epsilon = 10^{-4}$. Note also that the pseudo spikes of the x-variable during the active phase have nearly disappeared as predicted, with only vestigial spikes at the beginning and end of the plateau. For some values of ϵ and b_1, the pseudo-plateau bursting appears to be chaotic, exhibiting depolarized plateaus with variable and unpredictable duration. That is, the minimum of z lies at SN_2, but its maxima lie between HB_1 and SN_1. An example is shown in Fig. 9(b) with $s = -2.6$, $b_1 = -0.12$ and $\epsilon = 0.001$.

The Hopf bifurcation of the full system In all the examples that we showed of the bifurcation diagam of the full system Eqns. (1)–(3), the Hopf bifurcation HB_2 of the equilibrium FP happens at a relatively large value of ϵ. However, depending on the choice for b_1, which moves the location of FP on the Z-shaped steady-state curve at $\epsilon = 0$ relative to the HC of the fast subsystem, HB_2 can occur for arbitrarily small $0 < \epsilon \ll 1$. Figure 10 presents a two-parameter bifurcation diagram of the Hopf point HB_2 in dependence on b_1 and ϵ. The curves for both $s = -1.61$ and $s = -2.6$ are shown.

If we increase b_1 to 0 (this means going down in Fig. 10), starting from HB_2 at $b_1 = -0.01$ where FP lies below the HC at $\epsilon = 0$ for both choices of s (Figs. 3 and 4), the Hopf bifurcation curve ends at the saddle-node bifurcation SN_2 at $\epsilon = 0$. As discussed in Appendix A.2, the point SN_2 at $\epsilon = 0$ corresponds to a singular Hopf bifurcation of the full system, which persists for $0 < \epsilon \ll 1$, where it occurs at a value of b_1 for which FP lies $O(\epsilon)$ close to (but past) the left knee of the Z-shaped steady-state curve. The occurrence of a singular Hopf bifurcation has been shown previously for the original Hindmarsh-Rose system (25) in (2, Fig. 12) as

well as in (39); see also (24). Note that HB_2 is only a singular Hopf bifurcation for $0 < \epsilon \ll 1$ and $-1 \ll b_1 \leq 0$, but the exact transition from an ordinary to a singular Hopf bifurcation is not defined. When FP corresponds to a saddle very close to SN_2 at $\epsilon = 0$, it is unstable for $0 < \epsilon \ll 1$, but its two unstable eigenvalues are complex conjugate and lie extremely close to the imaginary axis. Hence, only a very small increase in ϵ already stabilizes FP as the singular Hopf bifurcation HB_2 occurs. The singular Hopf bifurcation gives rise to a small-amplitude periodic orbit that transforms very quickly as ϵ varies over an exponentially small interval; if HB_2 is supercritical, ϵ will be decreasing, but if HB_2 is subcritical the branch will turn around at an SNP bifurcation that happens exponentially close after HB_2. For the fold-homoclinic case, the periodic orbit transforms into an n-spike bursting orbit where n is extremely large for ϵ small. For the fold-subHopf case, the periodic oribt transforms into a relaxation oscillation. These exponentially small transitions involve so-called canard orbits, where the periodic orbits contain segments that follow the saddle-branch of the Z-shaped steady-state curve (24).

If we decrease b_1 from $b_1 = -0.01$, we find that the Hopf curve for both $s = -1.61$ and $s = -2.6$ initially increases in ϵ, but then decreases again until it ends at $\epsilon = 0$. However, the Hopf curve is not monotonic in b_1. Initially, the equilibrium FP moves up the middle branch at $\epsilon = 0$ and past SN_1 onto the upper branch of unstable equilibria until it reaches HB_1 at a value of $\epsilon > 0$. However, the Hopf curve continues for decreasing ϵ when we trace FP past HB_1 onto the stable segment of the upper branch of the Z-shaped curve. As ϵ decreases further, the Hopf curve reaches a minimum in b_1 (which corresponds to a maximum in Fig. 10) and then returns to the value of b_1 that corresponds to HB_1 as $\epsilon \to 0$. Hence, for a small range of b_1 when FP is located close to but to the left of HB_1 on the stable segment of the upper steady-state branch, there exists a small range of values $0 < \epsilon \ll 1$ for which FP loses stability and the attractor is a small-amplitude periodic orbit; the end points of this small interval are (ordinary) Hopf bifurcation points. However, when FP is unstable, only one Hopf bifurcation exists for $0 < \epsilon \ll 1$, which stabilizes FP as ϵ increases.

Note that in the fold-homoclinic case HB_1 is supercritical, while in the fold-subHopf case it is subcritical. Furthermore, HB_2 is subcritical when FP at $\epsilon = 0$ lies near SN_2 (see Fig. 3), but it is supercritical when FP at $\epsilon = 0$ lies near SN_1 (see Fig. 6). Hence, there must be at least one degenerate Hopf bifurcation on the *blue* curve ($s = -1.61$) corresponding to the fold-homoclinic case, and at least two degenerate Hopf bifurcations on the *red* curve ($s = -2.6$) corresponding to the fold-subHopf case in Fig. 10.

Discussion

Given the importance of the rapid ionic activities in endocrine cells that set the levels of $[\mathrm{Ca}^{2+}]_{\mathrm{i}}$ (5, 8, 48, 49) and are instrumental for the regulation of hormone exocytosis, it is of interest to identify the key mechanisms governing them.

We consider two general classes of models for endocrine bursting, square-wave bursting models (fold-homoclinic) and pseudo-plateau bursting models (fold-subHopf). It is important, in particular, to understand the similarities and differences between square-wave and pseudo-plateau bursting because they can be regarded as a form of plasticity of the intrinsic membrane properties and thus could have a profound effect on their function. We have presented here a generic Hodgkin-Huxley type model that captures the main features of a number of previously published models, which pointed to a possible physiological locus for the difference between the classes and also a simplified polynomial model, which emphasized the general dynamic features of the two classes of bursters and was more convenient for the challenging numerical continuations carried out here.

Physiological implications. Although we have focused on the mathematical effects of varying the parameter f_{c} (corresponding to ϵ in the simplified polynomial model), it represents the fraction of free cytosolic Ca^{2+} and accounts for the buffering capacity of cells. Smaller values of f_{c} slow down the rise in Ca^{2+} and in turn the activation of the K_{Ca} channels. As shown here, the cells exhibit bursts with more spikes and, hence, longer depolarized plateaus. This agrees with a recent study (37) that combined modeling and experiments to show that cytosolic calcium buffering capacity can tightly modulate neuronal firing patterns and determine whether bursting or spiking is generated. The range of parameter values ($f_{\mathrm{c}} \geq 10^{-3}, \epsilon \geq 10^{-3}$) we were able to explore numerically is comparable to that found in most previously published models (ranging from 10^{-3} to 10^{-1}) (11, 12, 16, 30, 40, 42, 45–47) and also observed in cells (1, 6, 9, 20, 21, 33, 35, 38, 52). Calcium buffering capacity is not only variable among cells but can change under different physiological conditions, such as the developmental stage. In a recent study in hippocampal granule cells, younger cells had approximately three times smaller Ca^{2+}-binding ratio (41) than older cells. We note that the unusually slow Ca^{2+} oscillations in pancreatic β-cells (periods from tens of seconds to several minutes) are likely not the result of very small binding ratio but rather reflect the slow dynamics of metabolism and/or of Ca^{2+} in the endoplasmic reticulum (12).

A key difference between the two types of bursters is that the spikes disappear in the fold-subHopf case as f_{c} or ϵ goes to 0. It may thus be possible to distinguish the two types experimentally by reducing ϵ via addition of exogenous Ca^{2+} buffer as in (37). This also sheds new light on a question raised by the early observation

that square-wave bursters are like relaxation oscillators with spikes superimposed on the upper state. Namely, if cells need a plateau to raise $[\mathrm{Ca}^{2+}]_{\mathrm{i}}$, why do they not just have a plateau instead of spikes? One possibility is that cells have to build the plateau out of ion channel interactions, and the delayed rectifier is too slow to cancel out the spikes and produce a pure plateau. In addition, given the naturally occurring range of f_{c} (10^{-3}–10^{-1}), Ca^{2+} is too fast compared to the rate of attraction to the upper state to eliminate the spikes. With the earlier fold-homoclinic models, this was not so apparent because the spike amplitude does not vary with f_{c}. In this sense, one can view fold-subHopf as a case that is closer to a plateau and in fact results in higher calcium, at least when mediated by a shift in $V_{\mathrm{m_L}}$.

Full-system bifurcation analysis and spike adding. In this paper we have examined both the square-wave and pseudo-plateau bursting regimes in terms of bifurcations of the full polynomial system over a relatively large range of ϵ. Similar analyses for small fixed ϵ and varying other parameters have been carried out previously for fold-homoclinic bursting (2, 7, 50), but we have treated fold-subHopf bursting for the first time. We considered the two together as they form a class of closely related biological systems.

We showed the emergence of bursting from a primordial large-amplitude spiking solution that undergoes a complicated cascade of bifurcations in the full system as the parameter ϵ decreases (Figs. 3–6). A classic period-doubling cascade that gives rise to two-, four- and higher-periodic orbits and presumably chaotic orbits spawns a cascade of spike-adding bifurcations that generates a sequence of new period-2,3,4,5,...,n attractors, for some finite number n, as ϵ decreases. The latter correspond to bursting trajectories with the respective number of spikes. The increase in the number of spikes as ϵ decreases has the geometric interpretation that, as the slow-variable component (the z-coordinate of the polynomial model) of the bursting orbits of the full system slows down, the trajectory spends more and more time moving along the z direction in phase space.

Previous studies have examined spike adding for fold-homoclinic bursting (2, 34, 43, 44, 50). Here, Figs. 4, 6 and 8(b) show that spike adding happens similarly as ϵ is reduced in the case of fold-subHopf bursting. We showed, in addition, for both types of bursters that the form of the transition depends on where the full-system steady state FP at $\epsilon = 0$ is located relative to the fast-subsystem HC. When FP at $\epsilon = 0$ lies well below the HC (a case that has been considered for fold-homoclinic bursters in (2, 34, 43, 44, 50)), the periodic branch is connected and the addition of each spike is marked by a pair of SNP bifurcations (Fig. 4). In contrast, when FP at $\epsilon = 0$ lies well above the HC, the periodic branch is disjoint,

with isolas and period-doubling bifurcations for each new spike (Fig. 6).

Further, as shown in Fig. 8, where FP at $\epsilon = 0$ and the HC are very close, the spike-adding transition appears to be of mixed type. Initially, as ϵ decreases the usual period-doubling cascade occurs that characterizes the transition mediated via isolas. However, we find no individual isolas for 3,4,5,..-spike solutions but a connected complicated periodic branch/isola that comprises these solutions and features saddle-node of periodics rather than period-doubling bifurcations. This suggests that there is a continuous transition between the two mechanisms of spike adding. Detailed analysis of this transition is left for future investigations as it requires analysis of the small ϵ-limit where our numerical computations break down.

Whereas the spike-adding cascades are similar for fold-homoclinic and fold-subHopf bursters, the two differ in their behaviors as $\epsilon \to 0$. As shown previously (7, 44), when FP at $\epsilon = 0$ lies above the HC, fold-homoclinic bursting must give way to small-amplitude continous spiking as $\epsilon \to 0$. In contrast, fold-subHopf bursters continues to exhibit large-amplitude oscillations as long as FP at $\epsilon = 0$ lies to the right of HB_1. Also, in the fold-subHopf case, the number of spikes increases to infinity as $\epsilon \to 0$ and their amplitude decreases to 0 because the rate of increase of the slow variable (z or Ca^{2+}) becomes much smaller than the rate of attraction to the branch of stable equilibria of the fast subsystem, culminating in plateaus with no spikes (Fig. 9(a)).

As in previous studies (34, 43, 44, 50), we also find bi-stability between regular bursting solutions with different numbers of spikes as well as multi-stability due to period-doubling cascades leading to chaos in the full system. As is the case for spike adding, the behavior differs depending on whether FP at $\epsilon = 0$ lies above or below HC. For example, in the case where spike adding is mediated via isolas (Figs. 5 and 6), regular bursting solutions with different numbers of spikes do not coexist. However, there are more complicated secondary bursting trajectories that do coexist with the regular bursting orbits and apparently chaotic alternation between such solutions can also be seen (Fig. 7(b)). In contrast, when the spike adding appears through SNP bifurcations (Figs. 3 and 4), there are small ranges for ϵ where both regular n- and $(n+1)$-spike bursting solutions, $n = 1, 2, 3, ...N$, are stable and again apparently chaotic alternation between such solutions is observed (Fig. 7(a)). These results agree well with previous work on fold-homoclinic bursting (2, 7, 14, 31, 32, 34, 39, 43, 44, 50) and are here extended to fold-subHopf bursters, which show the same behavior with respect to bi-stability and multi-stability.

Previous studies of spike adding have been done for the fold-homoclinic case by studying 1D Poincaré return maps or specially constructed 2D maps (2, 14, 31, 32, 34, 39, 44, 50), in contrast to our approach of continuing periodic orbits of the full ODE system. Several studies have also constructed bifurcation diagrams of the

full system of ODEs (2, 14, 18). Such studies have pointed to the importance of spike-adding transitions for the genesis of bursting from simple continuous spiking solutions. Most studies have used a primary bifurcation parameter that translates the slow-variable nullcline; Ca^{2+} pump rate or the conductance of K_{Ca} channels have been popular choices, motivated by the ability of these parameters to convert bursting to small-amplitude continuous spiking in the first biophysical model of fold-homoclinic bursting (16).

Taking these studies together with ours, we can identify three distinct transitions between bursting and spiking in the fold-homoclinic case. When ϵ is small, there is a transition from bursting to small-amplitude spiking as FP at $\epsilon = 0$ crosses the HC from below. In the limit as $\epsilon \to 0$, the transition occurs precisely when FP coincides with the saddle equilibrium that corresponds to the HC (7, 44), but bursting can persist when $\epsilon > 0$ for a range of FP loci above the HC. This is the second transition: when FP at $\epsilon = 0$ lies above the HC, spiking converts to bursting as ϵ increases from 0, passing through a complicated chaotic cascade along the way that includes plateaus of arbitrary and fluctuating duration (44). Finally, as ϵ becomes larger, the number of spikes per burst decreases, reaching a region of large-amplitude spiking (the third transition) before oscillations end in a Hopf bifurcation (HB_2 in Figs. 3–6 and 8). Those spiking solutions can be thought of as infinite trains of bursts with one spike, in contrast to the small-amplitude spiking above, which can be thought of as single bursts with an infinite number of spikes. Of the above transitions, only the third occurs in fold-subHopf bursting due to the lack of stable limit cycles in the fast subsystem.

Future directions. Our analysis is complementary to the study of Belykh et al. (7), who did a local analysis for small ϵ; namely, we consider the behavior at large ϵ. Fold-homoclinic bursting was addressed in their Scenario 3 and, as suggested above, fold-subHopf bursting has some similarities to their Scenario 1, though the latter is a pure relaxation oscillator with no Hopf bifurcation in the fast subsystem (HB_1 in our nomenclature).

We have identified one route to transform fold-homoclinic to fold-subHopf bursting, namely, translation of the activation curve of the Ca^{2+} current; there may be other parameters that can achieve this. Changing the conductance of voltage-gated K^+ channels or K_{Ca} channels, such as the BK channel, which is voltage- as well as Ca^{2+}-sensitive, can also shift the slow manifolds, change spike amplitude, and change the location and nature of the fast-subsystem Hopf bifurcations in endocrine cell models. BK blockade and natural variation of BK channel density were shown to affect the period of apparent pseudo-plateau bursting in pituitary somatotrophs (45), and BK blockade was shown to convert apparent bursting to

large amplitude spiking (47). Similar effects are seen by varying the time constant of voltage-gated K^+ channels or the conductance of voltage-dependent Ca^{2+} channels (unpublished observations). None of these changes has been seen to convert fold-subHopf to fold-homoclinic bursting or vice versa, though it is possible that they could do so in combination with other parameter changes. A promising framework in which to investigate these questions is that of Golubitsky et al. (23), where local unfoldings of singularities in the fast subsystem bifurcations were used to classify types of bursting.

Acknowledgments. AS was supported by the Intramural Research Program of NIDDK, National Institutes of Health, USA. HMO was supported by an Advanced Research Fellowship of the Engineering and Physical Sciences Research Council (EPSRC), UK. TR was supported by EPSRC grant EP/C544048/1. Both HMO and TR also received support from Cornell University via an IGERT grant of the National Science Foundation.

A Models and Methods

A.1 Generic Endocrine Model

The equations for the generic Hodgkin-Huxley-type model are:

$$C_{\rm m}\frac{dV_{\rm m}}{dt} = -(I_{\rm Ca}+I_{\rm K}+I_{\rm K_{Ca}}), \quad (4)$$

$$\frac{dn}{dt} = \frac{n_\infty(V_{\rm m})-n}{\tau_{\rm n}}, \quad (5)$$

$$\frac{dc}{dt} = -f_{\rm c}\,(\alpha\, I_{\rm Ca}(V_{\rm m})+k_{\rm PMCA}\,c), \quad (6)$$

where $C_{\rm m}$ is the membrane capacitance; $\tau_{\rm n}$ is the activation time constant for the delayed rectifier channel; n_∞ is the steady state function for the activation variable n; $C_{\rm m}=10^{-5}\times A_{\rm cell}$ is the membrane capacitance; $f_{\rm c}$ is the fraction of free to total cytosolic Ca^{2+}; $\alpha=10^5\ (2\times 9.65\times A_{\rm cell})^{-1}$ is a factor that converts current to flux, where $A_{\rm cell}=\pi\times d_{\rm cell}^2$ is the area of the cell; and $k_{\rm PMCA}$ is the plasma membrane Ca^{2+} ATPase pump rate. Since c represent the free Ca^{2+} concentration in the cytosol the corresponding fluxes in Eq. (6) are multiplied by the fraction $f_{\rm c}$ of free to total cytosolic Ca^{2+}. The currents included in the model equations are:

$$I_{\rm Ca}(V_{\rm m}) = g_{\rm Ca}\,m_\infty^2(V_{\rm m})\ (V_{\rm m}-V_{\rm Ca})\,, \quad (7)$$

$$I_{\rm K}(V_{\rm m},n) = g_{\rm K}\,n\ (V_{\rm m}-V_{\rm K})\,, \quad (8)$$

$$I_{\rm K_{Ca}}(V_{\rm m},c) = g_{\rm K_{Ca}}\,s_\infty(c)\ (V_{\rm m}-V_{\rm K})\,. \quad (9)$$

The steady state activation functions are:

$$m_\infty(V_\mathrm{m}) = \left(1+\exp\left(\frac{V_{\mathrm{m_L}}-V_\mathrm{m}}{s_m}\right)\right)^{-1}, \tag{10}$$

$$n_\infty(V_\mathrm{m}) = \left(1+\exp\left(\frac{V_\mathrm{n}-V_\mathrm{m}}{s_n}\right)\right)^{-1}, \tag{11}$$

$$s_\infty(c) = \frac{c^4}{c^4+k_\mathrm{s}^4}. \tag{12}$$

Values of all parameters used in the model simulations are given in Table A.1.

TABLE A.1
Parameter values of the Generic Pituitary Model

k_PMCA	20 s^{-1}	f_c	0.01
d_cell	10 μm	$g_\mathrm{K(Ca)}$	0.2 nS
V_K	-65 mV	g_Ca	0.81 nS
V_Ca	0 mV	g_K	2.25 nS
$V_{\mathrm{m_L}}$	-27.5 mV	V_n	0 mV
s_m	12 mV	s_n	8 mV
k_s	1.25 μM	τ_n	0.03 s^{-1}

A.2 Linear Stability Analysis of the Polynomial Model

According to Condition **C**6, the polynomial model Eqns. (1)–(3) has a unique equilibrium FP $= (x_\mathrm{FP}, y_\mathrm{FP}, z_\mathrm{FP})$ that exists for all $\epsilon \geq 0$. The location of FP is determined by the point where the z-nullcline intersects the Z-shaped steady-state curve of the fast subsystem Eqns. (1)–(2) at $\epsilon = 0$ and can be controlled by a single parameter. A convenient choice is the parameter b_1 as shown in Fig. 2. Hence, we assume that $a = 0.5$, $b = 1$, $a_1 = -0.1$, and $k = 0.2$ are fixed and s and b_1 may vary. By setting the right-hand sides of Eqns. (1)–(3) to 0, we find that FP is determined by the only real root x_FP of the polynomial equation

$$s\,k\,a\,x^3 - k\,(s+1)\,x^2 + s\,a_1\,b\,x + b_1\,b = 0. \tag{13}$$

The other coordinates of FP are given by

$$y_\mathrm{FP} = x_\mathrm{FP}^2, \quad \text{and} \quad z_\mathrm{FP} = \frac{s\,a\,x_\mathrm{FP}^3 - x_\mathrm{FP}^2\,(s+1)}{b} = \frac{s\,a_1\,x_\mathrm{FP} + b_1}{k}.$$

Note that for fixed values of a, b, a_1, and k the equilibrium FP depends on s and b_1 but not on ϵ. However, its stability does depend on ϵ (39). The Jacobian matrix of Eqns. (1)–(3) is given by

$$\mathbf{J} = \begin{pmatrix} \dfrac{\partial f}{\partial x} & \dfrac{\partial f}{\partial y} & \dfrac{\partial f}{\partial z} \\ \dfrac{\partial g}{\partial x} & \dfrac{\partial g}{\partial y} & 0 \\ \epsilon \dfrac{\partial h}{\partial x} & 0 & \epsilon \dfrac{\partial h}{\partial z} \end{pmatrix}.$$

The stability of FP is determined by the eigenvalues of $\mathbf{J}$ evaluated at FP. Hence, the eigenvalues are the roots of the characteristic polynomial

$$\begin{aligned} \mathbf{P}(\lambda) &= \left(\lambda - \epsilon \frac{\partial h}{\partial z}\right) \det \begin{pmatrix} \lambda - \dfrac{\partial f}{\partial x} & -\dfrac{\partial f}{\partial y} \\ -\dfrac{\partial g}{\partial x} & \lambda - \dfrac{\partial g}{\partial y} \end{pmatrix} - \\ &\qquad \epsilon \frac{\partial h}{\partial x} \det \begin{pmatrix} -\dfrac{\partial f}{\partial y} & -\dfrac{\partial f}{\partial z} \\ \lambda - \dfrac{\partial g}{\partial y} & 0 \end{pmatrix} \\ \Leftrightarrow \ \mathbf{P}(\lambda) &= \left(\lambda - \epsilon \frac{\partial h}{\partial z}\right) \det\left(\lambda \mathbf{I} - \mathbf{J_f}\right) - \epsilon \frac{\partial h}{\partial x} \frac{\partial f}{\partial z} \left(\lambda - \frac{\partial g}{\partial y}\right), \end{aligned} \quad (14)$$

where $\mathbf{J_f}$ is the Jacobian matrix of the fast subsystem Eqns. (1)–(2) evaluated at FP. For fixed $a = 0.5$, $b = 1$, $a_1 = -0.1$, and $k = 0.2$ the characteristic polynomial Eqn. (14) is given by

$$\begin{aligned} \mathbf{P}(\lambda) &= (\lambda + 0.2\,\epsilon)\,\left[(\lambda+1)\,(\lambda + 2\,s\,x_{\mathrm{FP}} - 1.5\,s\,x_{\mathrm{FP}}^2) + 2\,x_{\mathrm{FP}}\right] \\ &\quad +\epsilon\,a_1\,s\,(\lambda+1). \end{aligned} \quad (15)$$

We are primarily interested in the stability of FP for $0 < \epsilon \ll 1$ when FP is located on the unstable segments of the Z-shaped steady-state curve of the fast subsystem, that is, on the saddle segment with $\lambda_1 < 0 < \lambda_2$ that lies in between the two knees marked by saddle-node bifurcations (labeled SN_1 and SN_2 in Fig. 2) or on the segment of the upper branch with $\lambda_1, \lambda_2 > 0$ that lies after the Hopf bifurcation (labeled HB_1 in Fig. 2).

Note that the full system Eqns. (1)–(3) is degenerate at $\epsilon = 0$, because the Jacobian matrix $\mathbf{J}$ is then always singular. In the limit $\epsilon = 0$ Eqn. (14) reduces to

$$\mathbf{P}(\lambda) = -\lambda \det\left(\lambda \mathbf{I} - \mathbf{J_f}\right),$$

so that the eigenvalues of FP converge to the two eigenvalues $\lambda_{1,2}$ of $\mathbf{J_f}$ and the eigenvalue $\lambda_3 = 0$ as $\epsilon \to 0$. At $\epsilon = 0$, the characteristic polynomial $\mathbf{P}(\lambda)$ has two zero eigenvalues when FP lies on SN_1 (also $\lambda_1 = 0$) or SN_2 (also $\lambda_2 = 0$), and a pair of purely imaginary eigenvalues $\lambda_1 = \bar{\lambda}_2$ along with $\lambda_3 = 0$ when FP lies on HB_1.

If FP lies on the lower branch, before SN_2, then it is stable for $0 < \epsilon \ll 1$, that is, $\lambda_3 < 0$. As we decrease b_1 so that FP moves around the knee past SN_2, the eigenvalues $\lambda_2 < 0$ and $\lambda_3 < 0$ become complex conjugate and move through the imaginary axis, after which they become real again and $\lambda_2, \lambda_3 > 0$ (39). Hence, a Hopf bifurcation occurs that involves eigenvalues of both the fast (λ_2) and the slow (λ_3) equations. This is a singular Hopf bifurcation (13, 24). The characteristic polynomial Eqn. (14) for FP at SN_2, which corresponds to $b_1 = 0$ and FP $= (0, 0, 0)$ in Fig. 2 for both $s = -1.61$ and $s = -2.6$, becomes

$$\mathbf{P}(\lambda) = (\lambda + 1)\,(\lambda^2 + 0.2\,\epsilon\,\lambda + \epsilon\,a_1\,s),$$

and the eigenvalues are $\lambda_1 = -1$ and $\lambda_{2,3} = -0.1\,\epsilon \pm 0.1\,\sqrt{\epsilon^2 - 100\,\epsilon\,a_1\,s}$. Therefore, provided $\epsilon > 0$ is sufficiently small, $\lambda_{2,3}$ are complex conjugate with negative real parts. Thus, the singular Hopf bifurcation does not happen exactly when FP lies on SN_2, but when FP moves slightly past SN_2 onto the saddle-segment of the Z-shaped steady-state curve. Indeed, the theory predicts that the singular Hopf bifurcation lies $O(\epsilon)$ close to the point where FP passes through the knee (24).

As we continue to decrease b_1 and trace FP along the saddle-segment of the Z-shaped steady-state curve, the eigenvalues of FP are $\lambda_1 < 0 < \lambda_2$ and $\lambda_3 > 0$. Note that as FP reaches the homoclinic bifurcation point HC the sum $\lambda_1 + \lambda_2$ of the eigenvalues that converge to those of the fast subsystem for $\epsilon \to 0$ is negative for $s = -1.61$ and positive for $s = -2.6$. This is consistent with the type of the Hopf bifurcation in the fast subsystem, which is supercritical in the case of fold-homoclinic bursting ($s = -1.61$) and subcritical in the case of fold-subHopf ($s = -2.6$).

When FP moves around the right knee past SN_1, one typically expects another singular Hopf bifurcation (39). However, we fixed $a = 0.5$, $b = 1$, $a_1 = -0.1$, and $k = 0.2$ such that there is only one Hopf bifurcation on the upper branch of the Z-shaped steady-state curve. This means that the equilibria of the fast subsystem are unstable on both sides of SN_1. For b_1 such that FP is located $O(\epsilon)$ away from SN_1 on the middle branch of the Z-shaped curve, the eigenvalues of FP are $\lambda_1 < 0 < \lambda_2$ and $\lambda_3 > 0$, while for FP located $O(\epsilon)$ away from SN_1 on the upper branch of the Z-shaped curve, its eigenvalues are $\lambda_1, \lambda_2 > 0$ and $\lambda_3 < 0$. Hence, in our case, it is not possible to get a singular Hopf bifurcation. Numerical calculations for $s = -2.6$ and $\epsilon = 10^{-6}$ seem to indicate that λ_1 and λ_3 pass through

zero simultaneously, though generically, one would expect that they do so via two subsequent saddle-node bifurcations. However, none of the eigenvalues ever become zero ($\det \mathbf{J} \neq 0$) when $\epsilon > 0$ and either $s = -2.6$ or $s = -1.61$; indeed, the degeneracy at SN_1 needs further investigation, but this is beyond the scope of this paper.

When b_1 is such that FP lies in between HB_1 and SN_1 then FP is a saddle with two unstable eigenvalues ($\lambda_3 < 0$ for $0 < \epsilon \ll 1$). As b_1 decreases from a value with FP located close to SN_1, the eigenvalues λ_1 and λ_2 that correspond to the fast subsystem coalesce on the real axis and become complex conjugate with positive real parts. This marks a transition from saddle-node to saddle-focus equilibrium. Finally, another Hopf bifurcation occurs as FP passes through HB_1, but this is not a singular Hopf bifurcation because it involves only eigenvalues corresponding to the fast subsystem.

A.3 Computational method

The models simulations were done with the software package XPPAUT (19). The bifurcation analysis was performed with AUTO (17).

References

[1] Al-Baldawi, N. & Abercrombie, R. (1995). Cytoplasmic calcium buffer capacity determined with Nitr-5 and DM-nitrophen. *Cell Calcium,* **17** (6), 409–421.

[2] Alexander, J. & Cai, D. (1991). On the dynamics of bursting systems. *J Math Biol,* **29** (5), 405–23.

[3] Baer, S. M., Erneux, T. & Rinzel, J. (1989). The slow passage through a Hopf bifurcation: delay, memory effects, and resonance. *SIAM Journal on Applied Mathematics,* **49** (1), 55–71.

[4] Barg, S. & Rorsman, P. (2004). Insulin Secretion: A High-affinity Ca^{2+} Sensor After All? *J. Gen. Physiol.* **124** (6), 623–625.

[5] Beauvois, M. C., Merezak, C., Jonas, J.-C., Ravier, M. A., Henquin, J.-C. & Gilon, P. (2006). Glucose-induced mixed $[Ca^{2+}]_c$ oscillations in mouse beta-cells are controlled by the membrane potential and the SERCA3 Ca^{2+}-ATPase of the endoplasmic reticulum. *Am J Physiol Cell Physiol,* **290** (6), C1503–1511.

[6] Belan, P., Kostyuk, P., Snitsarev, V. & Tepikin, A. (1993). Calcium clamp in isolated neurones of the snail Helix pomatia. *The Journal of Physiology,* **462** (1), 47–58.

[7] Belykh, V., Belykh, I., Colding-Jørgensen, M. & Mosekilde, E. (2000). Homoclinic bifurcations leading to the emergence of bursting oscillations in cell models. *The European Physical Journal E,* **3** (3), 205–219.

[8] Bergsten, P. (2002). Role of Oscillations in Membrane Potential, Cytoplasmic Ca^{2+}, and Metabolism for Plasma Insulin Oscillations. *Diabetes,* **51** (90001), S171–176.

[9] Berlin, J., Bassani, J. & Bers, D. (1994). Intrinsic cytosolic calcium buffering properties of single rat cardiac myocytes. *Biophysical Journal,* **67** (4), 1775–1787.

[10] Bertram, R., Butte, M., Kiemel, T. & Sherman, A. (1995). Topological and phenomenological classification of bursting oscillations. *Bull Math Biol,* **57** (3), 413–39.

[11] Bertram, R., Previte, J., Sherman, A., Kinard, T. & Satin, L. (2000). The phantom burster model for pancreatic beta-cells. *Biophys J,* **79** (6), 2880–92.

[12] Bertram, R. & Sherman, A. (2004). A calcium-based phantom bursting model for pancreatic islets. *Bull Math Biol,* **66** (5), 1313–44.

[13] Braaksma, B. (1998). Singular hopf bifurcation in systems with fast and slow variables. *J. Nonlinear Sci.* **8**, 457–490.

[14] Channell, P., Cymbalyuk, G. & Shilnikov, A. (2007). Origin of bursting through homoclinic spike adding in a neuron model. *Physical Review Letters,* **98** (13), 134101.

[15] Chay, T. (1986). On the effect of the intracellular calcium-sensitive K^{+} channel in the bursting pancreatic β-cell. *Biophysical Journal,* **50** (5), 765 – 777.

[16] Chay, T. & Keizer, J. (1983). Minimal model for membrane oscillations in the pancreatic beta-cell. *Biophysical Journal,* **42** (2), 181–189.

[17] Doedel, E., , Champneys, A., Fairgrieve, T., Kuznetsov, Y., Sandstede, B. & Wang, X. (1997). AUTO97: continuation and bifurcation software for ordinary differential equations (with HomCont). User's guide Concordia Univ.

[18] Duan, L., Lu, Q. & Wang, Q. (2008). Two-parameter bifurcation analysis of firing activities in the Chay neuronal model. *Neurocomputing,* **72** (1-3), 341 – 351.

[19] Ermentrout, B. (2002). *Simulating, Analyzing and Animating Dynamical Systems: A Guide to* XPPAUT *for Researchers and Students.* SIAM.

[20] Fierro, L. & Llano, I. (1996). High endogenous calcium buffering in Purkinje cells from rat cerebellar slices. *The Journal of Physiology,* **496** (3), 617–625.

[21] Fleet, A., Ellis-Davies, G. & Bolsover, S. (1998). Calcium buffering capacity of neuronal cell cytosol measured by flash photolysis of calcium buffer NP-EGTA. *Biochemical and Biophysical Research Communications,* **250** (3), 786–790.

[22] Goforth, P., Bertram, R., Khan, F., Zhang, M., Sherman, A. & Satin, L. (2002). Calcium-activated K^+ channels of mouse beta-cells are controlled by both store and cytoplasmic Ca^{2+}: experimental and theoretical studies. *J Gen Physiol,* **120** (3), 307–22.

[23] Golubitsky, M., Josic, K. & Kaper, T. (2001). An unfolding theory approach to bursting in fast-slow systems. In *Global Analysis of Dynamical Systems: Festschrift dedicated to Floris Takens for his 60th birthday*, (Broer, HW and Krauskopf, B and Vegter, G, ed.), pp. 277–308, Institute of Physics Publishing.

[24] Guckenheimer, J. (2008). Singular hopf bifurcation in systems with two slow variables. *SIAM J. Appl. Dyn. Syst.* **7** (4), 1355–1377.

[25] Hindmarsh, J. & Rose, R. (1984). A model of neuronal bursting using 3 coupled 1st order differential-equations. *Proceedings of the Royal Society of London Series B-Biological Sciences,* **221** (1222), 87–102.

[26] Hodgkin, A. & Huxley, A. (1952). A quantitative description of membrane current and its application to conduction and excitation in nerve. *Journal of Physiology-London,* **117** (4), 500–544.

[27] Izhikevich, E. (2000). Neural excitability, spiking and bursting. *International Journal of Bifurcation and Chaos,* **10** (6), 1171–1266.

[28] Izhikevich, E. M. (2007). *Dynamical systems in neuroscience : the geometry of excitability and bursting*. Computational neuroscience, MIT Press, Cambridge, Mass.

[29] Jonas, J., Gilon, P. & Henquin, J. (1998). Temporal and quantitative correlations between insulin secretion and stably elevated or oscillatory cytoplasmic Ca^{2+} in mouse pancreatic β-cells. *Diabetes,* **47** (8), 1266–1273.

[30] LeBeau, A. P., Robson, A. B., McKinnon, A. E. & Sneyd, J. (1998). Analysis of a reduced model of cortiocotroph action potentials. *Journal of Theoretical Biology,* **192** (3), 319 – 339.

[31] Medvedev, G. S. (2005). Reduction of a model of an excitable cell to a one-dimensional map. *Physica D: Nonlinear Phenomena,* **202** (1-2), 37 – 59.

[32] Medvedev, G. S. (2006). Transition to bursting via deterministic chaos. *Physical Review Letters,* **97** (4).

[33] Müller, T., Partridge, L. & Swandulla, D. (1993). Calcium buffering in bursting Helix pacemaker neurons. *Pflügers Archiv European Journal of Physiology,* **425** (5), 499–505.

[34] Mosekilde, E., Lading, B., Yanchuk, S. & Maistrenko, Y. (2001). Bifurcation structure of a model of bursting pancreatic cells. *Biosystems,* **63** (1-3), 3 – 13.

[35] Neher, E. & Augustine, G. (1992). Calcium gradients and buffers in bovine chromaffin cells. *The Journal of Physiology,* **450** (1), 273–301.

[36] Rinzel, J. (1985). Bursting oscillations in an excitable membrane model. In *Lecture Notes in Mathematics* vol. 1151, pp. 304–316.

[37] Roussel, C., Erneux, T., Schiffmann, S. & Gall, D. (2006). Modulation of neuronal excitability by intracellular calcium buffering: from spiking to bursting. *Cell Calcium,* **39** (5), 455 – 466.

[38] Schwiening, C. & Thomas, R. (1996). Relationship between intracellular calcium and its muffling measured by calcium iontophoresis in snail neurones. *The Journal of Physiology,* **491** (3), 621–633.

[39] Shilnikov, A. & Kolomiets, M. (2008). Methods of the qualitative theory for the Hindmarsh-Rose model: A case study. A tutorial. *International Journal of Bifurcation and chaos,* **18** (8), 2141–2168.

[40] Stern, J., Osinga, H., LeBeau, A. & Sherman, A. (2008). Resetting behavior in a model of bursting in secretory pituitary cells: distinguishing plateaus from pseudo-plateaus. *Bull Math Biol,* **70** (1), 68–88.

[41] Stocca, G., Schmidt-Hieber, C. & Bischofberger, J. (2008). Differential dendritic Ca^{2+} signalling in young and mature hippocampal granule cells. *The Journal of Physiology,* **586** (16), 3795–3811.

[42] Tabak, J., Toporikova, N., Freeman, M. & Bertram, R. (2007). Low dose of dopamine may stimulate prolactin secretion by increasing fast potassium currents. *J Comput Neurosci,* **22** (2), 211–22.

[43] Terman, D. (1991). Chaotic spikes arising from a model of bursting in excitable-membranes. *SIAM Journal on Applied Mathematics,* **51** (5), 1418–1450.

[44] Terman, D. (1992). The transition from bursting to continuous spiking in excitable membrane models. *Journal of Nonlinear Science,* **2** (2), 135–182.

[45] Tsaneva-Atanasova, K., Sherman, A., van Goor, F. & Stojilkovic, S. (2007). Mechanism of spontaneous and receptor-controlled electrical activity in pituitary somatotrophs: experiments and theory. *Journal of Neurophysiology,* **98** (1), 131–144.

[46] Tsaneva-Atanasova, K., Zimliki, C., Bertram, R. & Sherman, A. (2006). Diffusion of calcium and metabolites in pancreatic islets: killing oscillations with a pitchfork. *Biophys J,* **90** (10), 3434–46.

[47] Van Goor, F., Li, Y. & Stojilkovic, S. (2001*a*). Paradoxical role of large-conductance calcium-activated K^+ (BK) channels in controlling action potential-driven Ca^{2+} entry in anterior pituitary cells. *J Neurosci,* **21** (16), 5902–15.

[48] Van Goor, F., Zivadinovic, D., Martinez-Fuentes, A. & Stojilkovic, S. (2001*b*). Dependence of pituitary hormone secretion on the pattern of spontaneous voltage-gated calcium influx. cell type-specific action potential secretion coupling. *J Biol Chem,* **276** (36), 33840–6.

[49] Vincent, J., Kukstas, L. & Lledo, P. (1992). Endocrine cell excitability opens the way to novel pharmacological intervention: example of the anterior pituitary cell. *Cell Biol Toxicol,* **8** (3), 85–91.

[50] Wang, X.-J. (1993). Genesis of bursting oscillations in the Hindmarsh-Rose model and homoclinicity to a chaotic saddle. *Phys. D,* **62** (1-4), 263–274.

[51] Zhang, M., Goforth, P., Bertram, R., Sherman, A. & Satin, L. (2003). The Ca^{2+} dynamics of isolated mouse beta-cells and islets: implications for mathematical models. *Biophys J,* **84** (5), 2852–70.

[52] Zhou, Z. & Neher, E. (1993). Mobile and immobile calcium buffers in bovine adrenal chromaffin cells. *The Journal of Physiology,* **469** (1), 245–273.

Figure Legends

Figure 1. Bifurcation diagrams of the fast subsystem in the generic endocrine model (Appendix A.1) showing the bifurcations associated with square-wave (fold-homoclinic) bursting (panel *a*) and pseudo-plateau (fold-subHopf) bursting (panel *b*). (a) $V_{\mathrm{m_L}} = -22.5$ mV; (b) $V_{\mathrm{m_L}} = -27.5$ mV; HB — Hopf bifurcation; SN — saddle-node bifurcation; SNP — saddle-node of periodics; HC — homoclinic bifurcation point. Dashed lines denote instability. Sample bursting trajectories are superimposed on the bifurcation diagrams for each of the models.

Figure 2. Bifurcation diagrams of the fast subsystem in the polynomial model Eqns. (1)–(2) showing the bifurcations associated with the transition from square-wave (fold-homoclinic) to pseudo-plateau (fold-subHopf) bursting as well as the z-nullcline for three different values of the parameter b_1 and with (a) $s = -1.6$, or (b) $s = -2.6$; HB — Hopf bifurcation; SN — saddle-node bifurcation; HC — homoclinic bifurcation point. Dashed lines denote instability.

Figure 3. (a) Three-dimensional view (ϵ, z, x) of the one-parameter bifurcation diagram with respect to ϵ of the full polynomial model Eqns. (1)–(3) in the case of square-wave bursting ($s = -1.6$, $b_1 = -0.01$); HB — Hopf bifurcation; SNP — saddle-node of periodics; FP — fixed point; HC — homoclinic bifurcation point. Dashed lines denote instability; (b) Sample bursting trajectories with increasing number of spikes, i.e., decreasing values of $\epsilon = 0.009;\ 0.005;\ 0.004;\ 0.0035;\ 0.0027;\ 0.0024;\ 0.002$ are superimposed on the bifurcation diagram.

Figure 4. (a) Bifurcation diagram of the full polynomial model Eqns. (1)–(3) with respect to ϵ in the case of pseudo-plateau bursting ($s = -2.6$, $b_1 = -0.01$); HB — Hopf bifurcation; SNP — saddle-node of periodics; FP — fixed point; PD — period-doubling bifurcation; HC — homoclinic bifurcation point. Dashed lines denote instability; (b) Sample bursting trajectories with increasing number of spikes, i.e., decreasing values of $\epsilon = 0.08;\ 0.06;\ 0.035;\ 0.023$ are superimposed on the bifurcation diagram.

Figure 5. (a) Bifurcation of the full polynomial model Eqns. (1)–(3) in the case of square-wave bursting ($s = -1.6$, $b_1 = -0.05$); HB — Hopf bifurcation; PD — period-doubling bifurcation; FP — fixed point; HC — homoclinic bifurcation point. Dashed lines denote instability; (b) Sample bursting trajectories with increasing number of spikes, i.e., decreasing values of

$\epsilon = 0.07;\ 0.04;\ 0.03;\ 0.024;\ 0.018;\ 0.015;\ 0.014;\ 0.012$ are superimposed on the bifurcation diagram.

Figure 6. (a) Bifurcation diagram of the full polynomial model Eqns. (1)–(3) in the case of pseudo-plateau bursting ($s = -2.6$, $b_1 = -0.21$); HB — Hopf bifurcation; PD — period-doubling bifurcation; FP — fixed point; SNP — saddle-node of periodics; HC — homoclinic bifurcation point. Dashed lines denote instability; (b) Sample bursting trajectories with increasing number of spikes, i.e., decreasing values of $\epsilon = 1.105;\ 0.9;\ 0.6;\ 0.4;\ 0.25;\ 0.15$ are superimposed on the bifurcation diagram.

Figure 7. Simulations of the polynomial model showing the apparently chaotic spike-adding transition in the pseudo-plateau bursting regime in the case when (a) FP is well below the HC ($s = -2.6$, $b_1 = -0.01$); and (b) when FP is well above the HC ($s = -2.6$, $b_1 = -0.21$).

Figure 8. Bifurcation diagrams of the full polynomial model Eqns. (1)–(3) in the cases of (a) square-wave bursting ($s = -1.6$, $b_1 = -0.024$); and (b) pseudo-plateau bursting ($s = -2.6$, $b_1 = -0.066$); HB — Hopf bifurcation; PD — period-doubling bifurcation; FP — fixed point; SNP — saddle-node of periodics; HC — homoclinic bifurcation point. Dashed lines denote instability.

Figure 9. Simulations showing the behavior in the pseudo-plateau bursting regime for small ϵ in the cases (a) when FP is well below the HC ($s = -2.6$, $b_1 = -0.01$, ϵ = 0.0001); and (b) when FP is above the HC but below SN_1 ($s = -2.6$, $b_1 = -0.12$, $\epsilon = 0.001$).

Figure 10. Three-dimensional view (ϵ, z, $-b_1$) of the two-parameter bifurcation diagram of the full polynomial model with respect to ϵ and b_1 showing the loci of HB_2 for $s = -1.6$ (blue) and $s = -2.6$ (red); HB — Hopf bifurcation; SN — saddle-node bifurcation. The vertical, dashed lines show the z-values of the hopf bifurcation HB_1 of the fast subsystem (ϵ = 0).

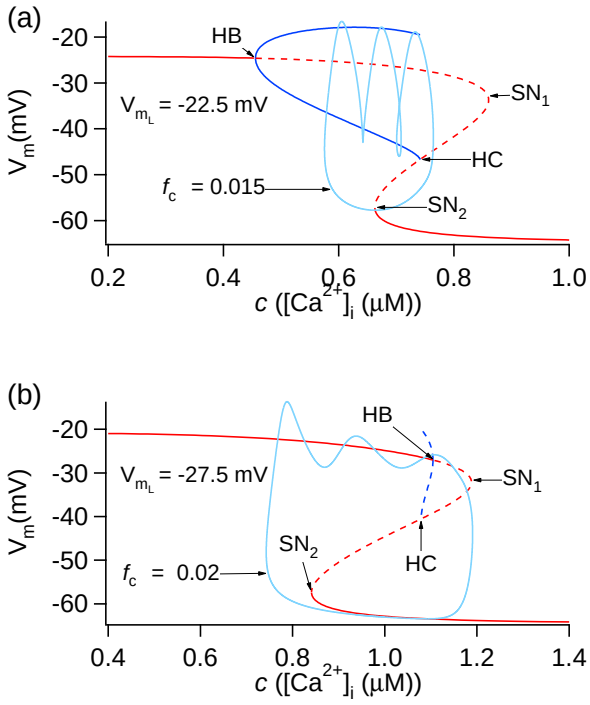
(a)
HB
SN1
V_mL = -22.5 mV
HC
f_c = 0.015
SN2
V_m(mV)
-20
-30
-40
-50
-60
0.2
0.4
0.6
0.8
1.0
c ([Ca2+]_i (μM))
(b)
HB
V_mL = -27.5 mV
SN1
SN2
HC
f_c = 0.02
V_m(mV)
-20
-30
-40
-50
-60
0.4
0.6
0.8
1.0
1.2
1.4
c ([Ca2+]_i (μM))

Figure 1:

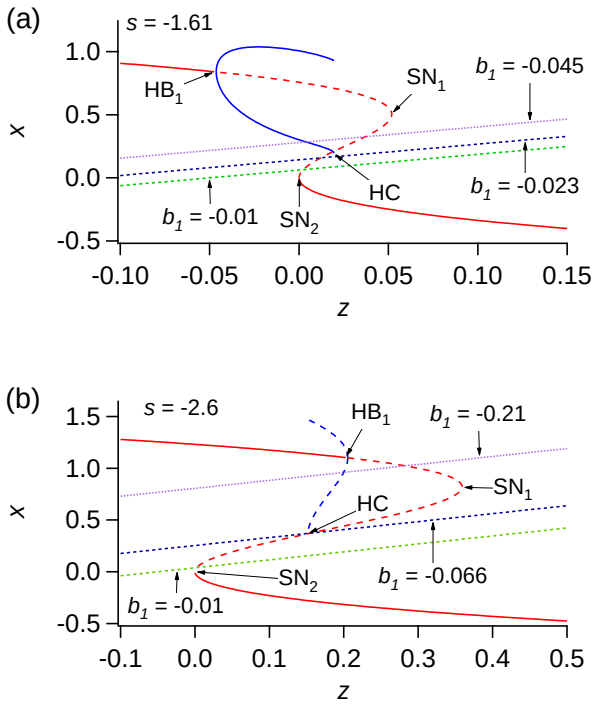
(a)
s = -1.61
HB1
SN1
b1 = -0.045
HC
b1 = -0.023
b1 = -0.01
SN2
x
z
(b)
s = -2.6
HB1
b1 = -0.21
SN1
HC
SN2
b1 = -0.066
b1 = -0.01
x
z

Figure 2:

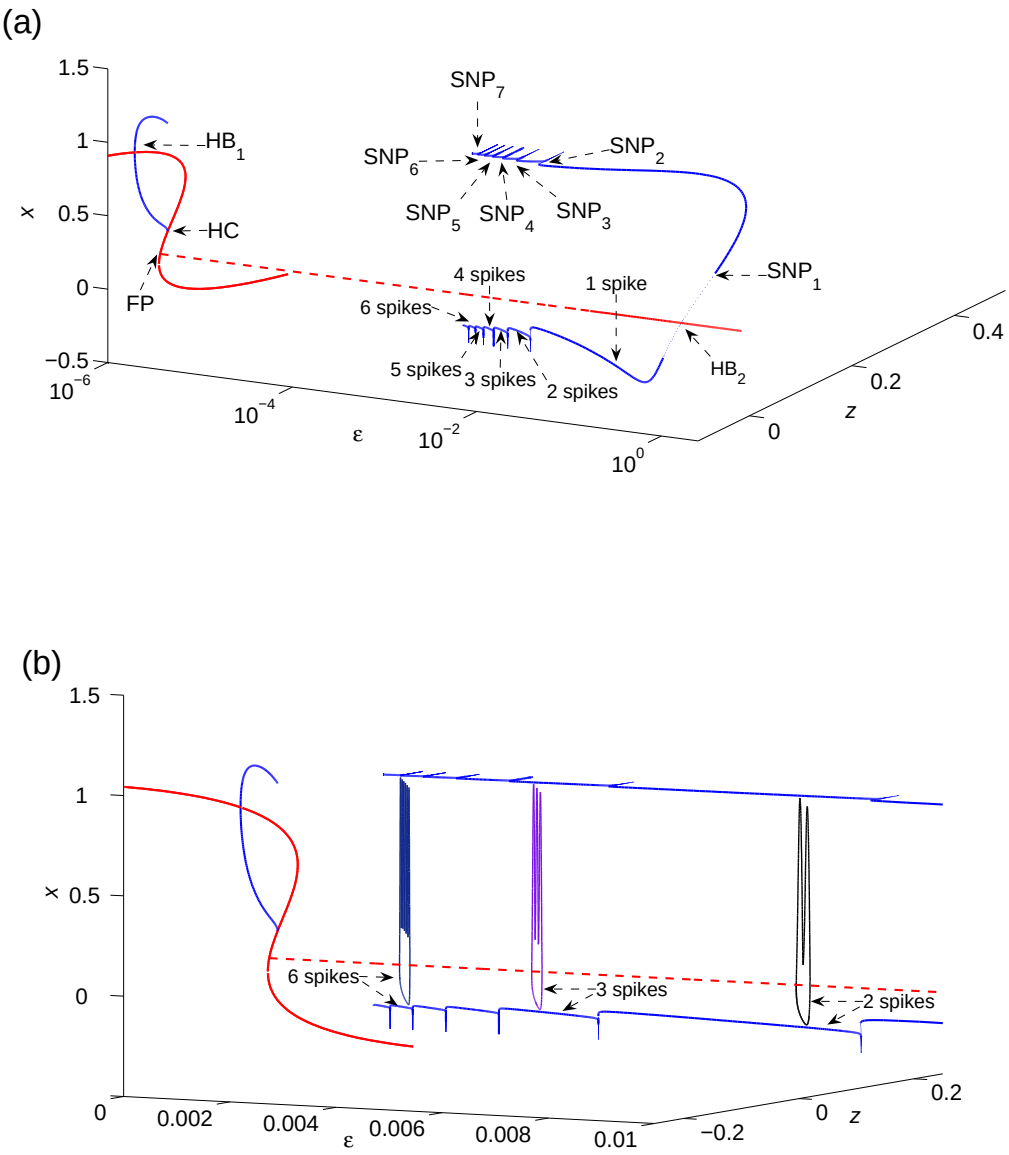
(a)
1.5
1
0.5
0
−0.5
x
HB1
HC
FP
SNP7
SNP6
SNP2
SNP5
SNP4
SNP3
4 spikes
1 spike
6 spikes
SNP1
5 spikes
3 spikes
2 spikes
HB2
10−6
10−4
10−2
100
ε
0
0.2
0.4
z
(b)
1.5
1
0.5
0
x
6 spikes
3 spikes
2 spikes
0
0.002
0.004
0.006
0.008
0.01
ε
−0.2
0
0.2
z

Figure 3:

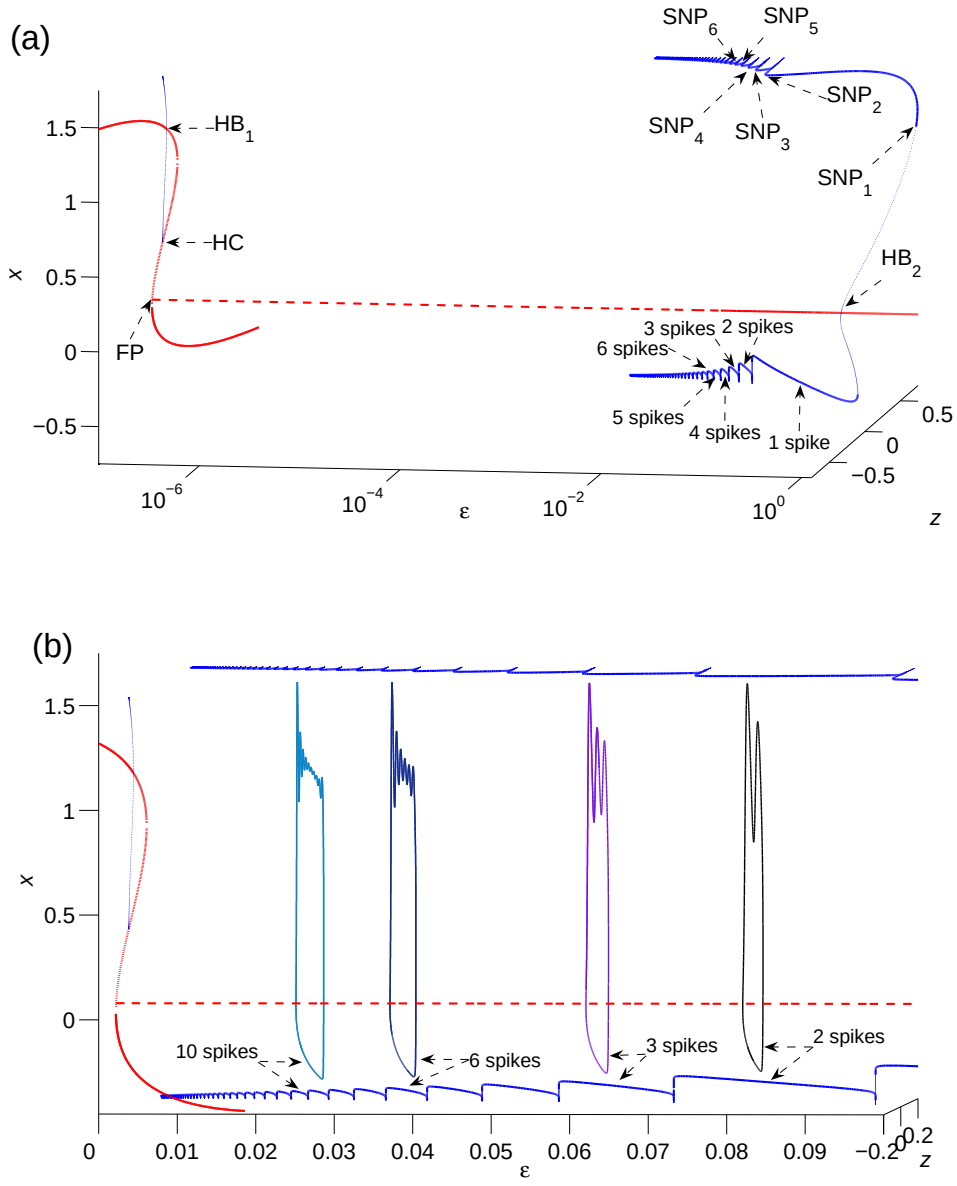
(a)
SNP6
SNP5
SNP2
SNP4
SNP3
SNP1
HB1
HC
HB2
FP
3 spikes
2 spikes
6 spikes
5 spikes
4 spikes
1 spike
1.5
1
0.5
0
−0.5
x
10−6
10−4
10−2
100
ε
0.5
0
−0.5
z
(b)
1.5
1
0.5
0
x
10 spikes
6 spikes
3 spikes
2 spikes
0
0.01
0.02
0.03
0.04
0.05
0.06
0.07
0.08
0.09
ε
0.2
0
−0.2
z

Figure 4:

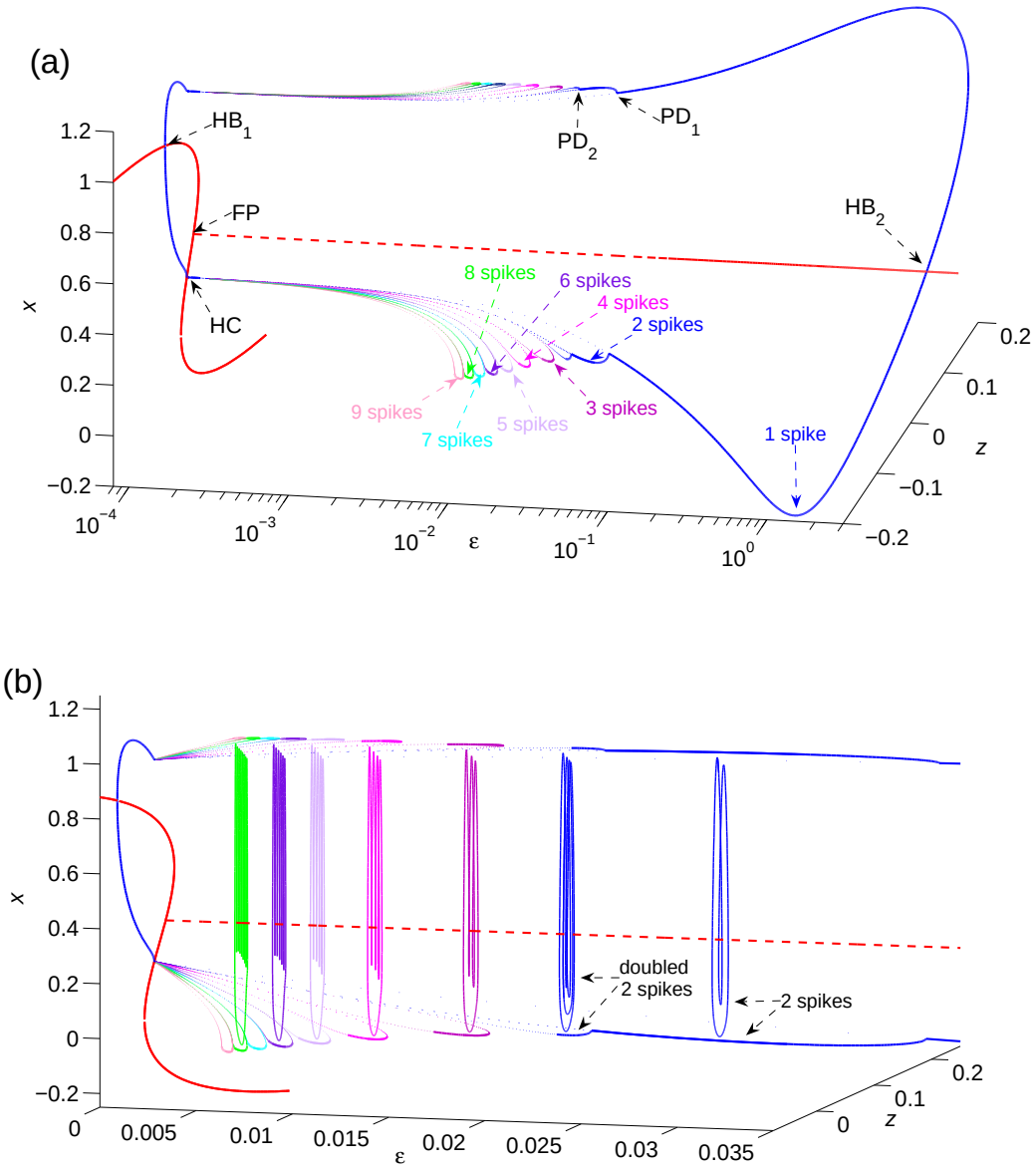
(a)
HB1
PD2
PD1
HB2
FP
HC
8 spikes
6 spikes
4 spikes
2 spikes
9 spikes
7 spikes
5 spikes
3 spikes
1 spike
x
ε
z
(b)
doubled
2 spikes
2 spikes

Figure 5:

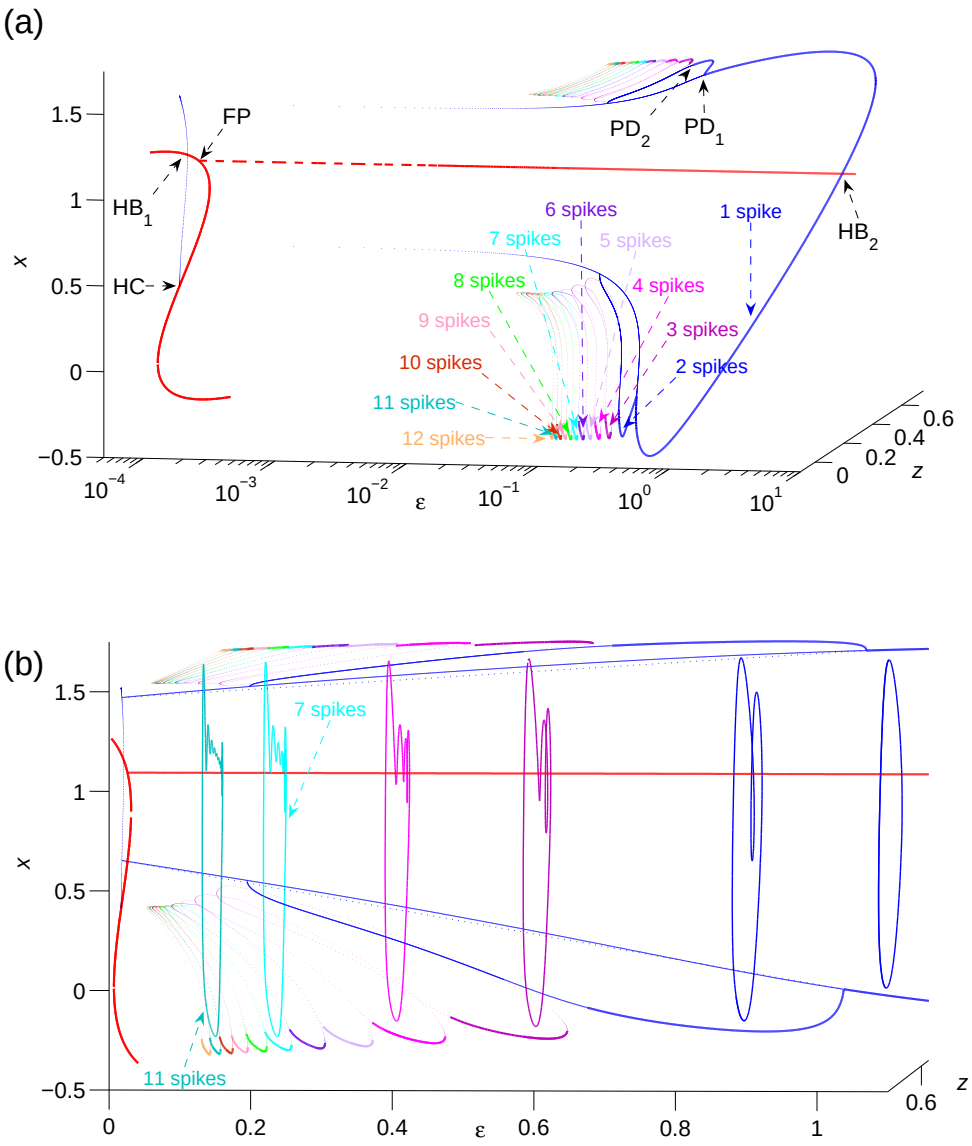
(a)
1.5
1
0.5
0
−0.5
x
FP
HB1
HC
PD2
PD1
HB2
6 spikes
7 spikes
5 spikes
1 spike
8 spikes
4 spikes
9 spikes
3 spikes
10 spikes
2 spikes
11 spikes
12 spikes
10−4
10−3
10−2
ε
10−1
100
101
0
0.2
0.4
0.6
z
(b)
1.5
1
0.5
0
−0.5
x
7 spikes
11 spikes
0
0.2
0.4
ε
0.6
0.8
1
0.6
z

Figure 6:

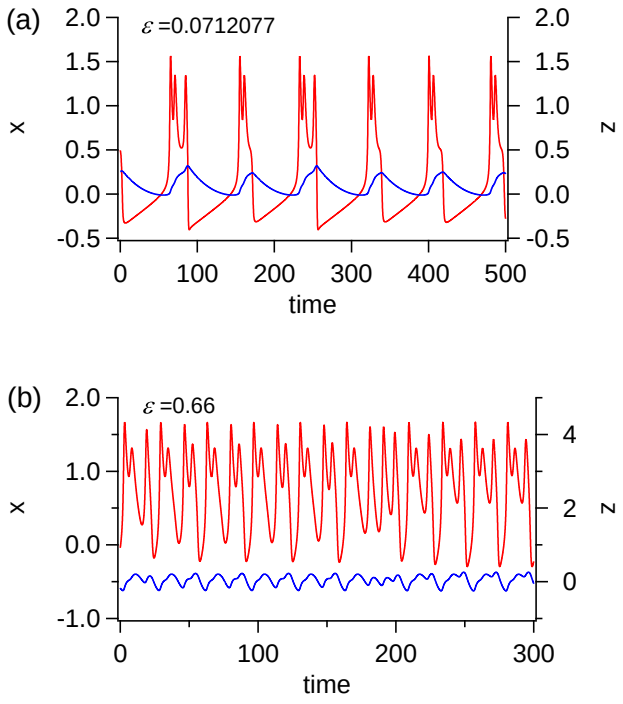

Figure 7:

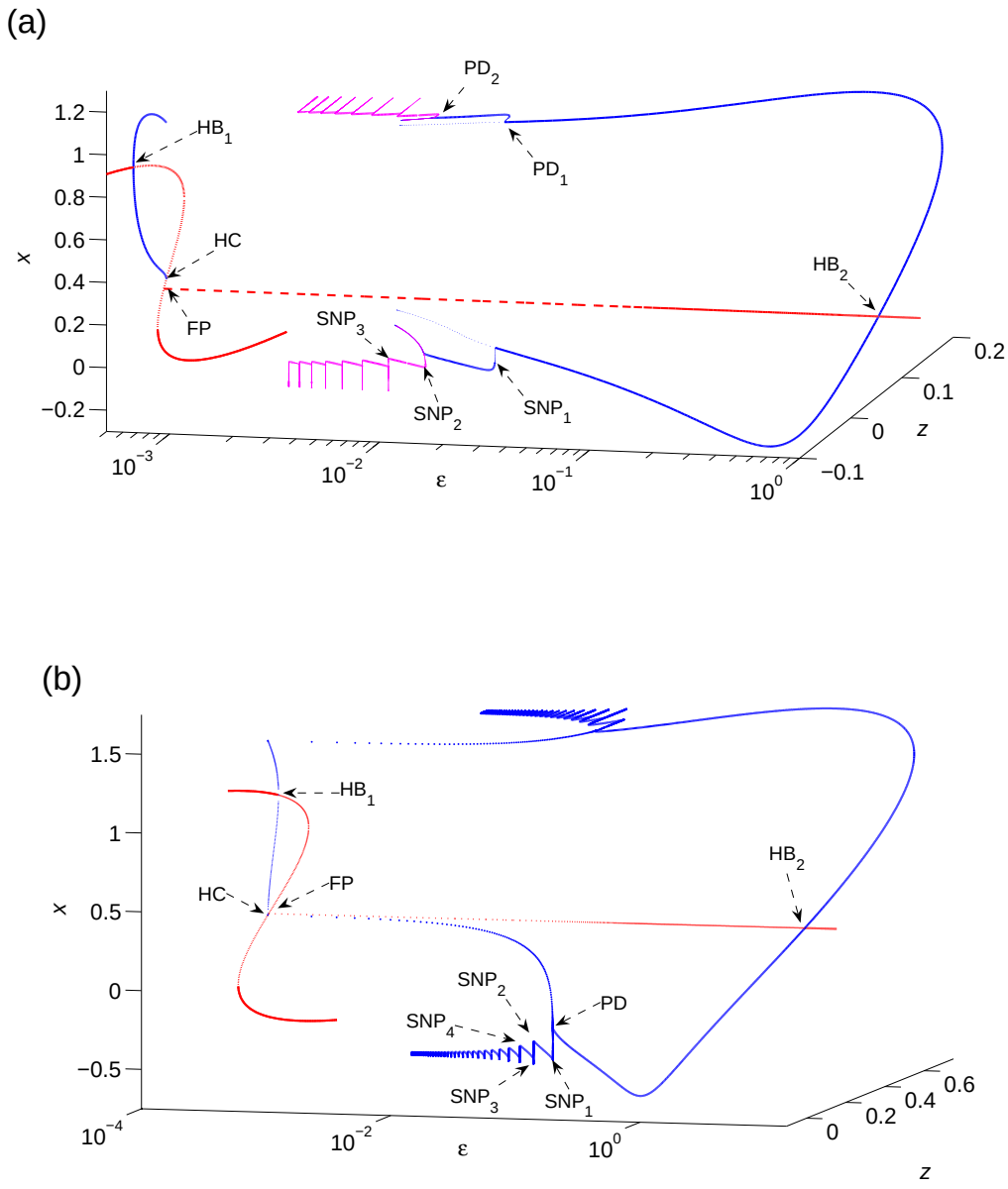
(a)
PD2
PD1
HB1
HC
FP
HB2
SNP3
SNP2
SNP1
1.2
1
0.8
0.6
0.4
0.2
0
−0.2
x
10−3
10−2
ε
10−1
100
0.2
0.1
0
z
−0.1
(b)
HB1
HC
FP
HB2
SNP2
PD
SNP4
SNP3
SNP1
1.5
1
0.5
0
−0.5
x
10−4
10−2
ε
100
0
0.2
0.4
0.6
z

Figure 8:

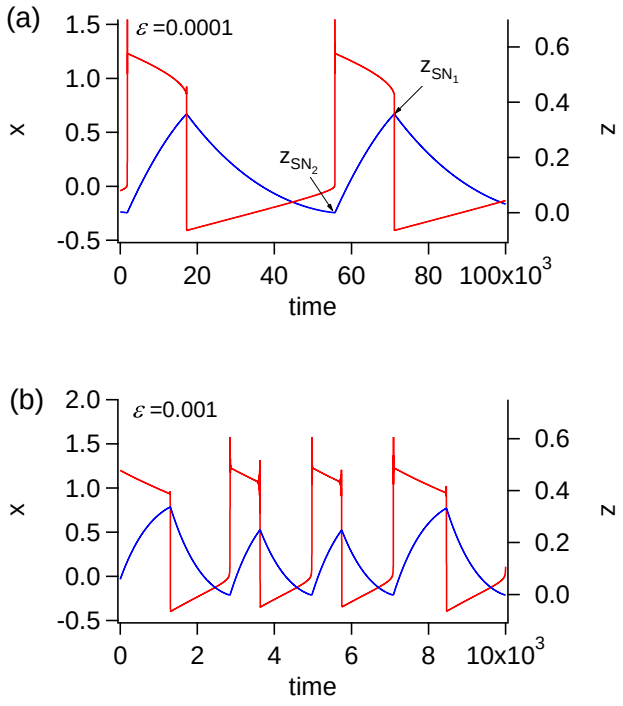

Figure 9:

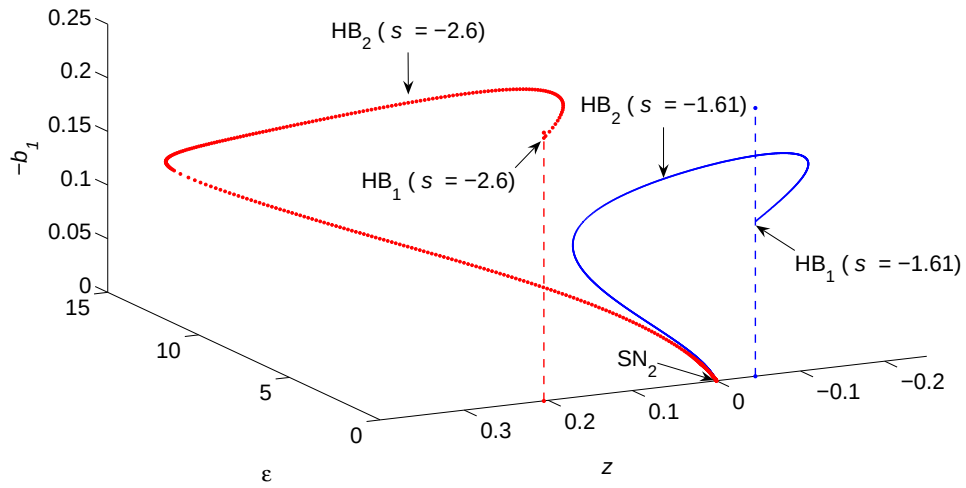
0.25
0.2
0.15
0.1
0.05
0
$-b_1$
15
10
5
0
ε
HB_2 (s = −2.6)
HB_1 (s = −2.6)
HB_2 (s = −1.61)
HB_1 (s = −1.61)
SN_2
0.3
0.2
0.1
0
−0.1
−0.2
z

Figure 10: